JOURNAL OF GEOPHYSICAL RESEARCH, VOL. 112, B07409, doi:10.1029/2006JB004399, 2007

Modeling afterslip and aftershocks following the 1992 Landers earthquake

H. Perfettini[1] and J.-P. Avouac[2]

Received 17 March 2006; revised 9 March 2007; accepted 4 April 2007; published 19 July 2007.

[1] One way to probe the rheology of the lithosphere and fault zones is to analyze the temporal evolution of deformation following a large earthquake. In such a case, the lithosphere responds to a known stress change that can be assessed from earthquake slip models constrained from seismology and geodesy. Here, we model the postseismic response of a fault zone that is assumed to obey a rate-strengthening rheology, where the frictional stress varies as $a\sigma \ln(\dot{\epsilon})$, $\dot{\epsilon}$ being the deformation rate and $a\sigma > 0$ a rheological parameter. The model is simple enough that these parameters can be estimated by inversion of postseismic geodetic data. We apply this approach to the analysis of geodetic displacements following the M_w7.3, 1992, Landers earthquake. The model adjusts well the measured displacements and implies $a\sigma \approx 0.47–0.53$ MPa. In addition, we show that aftershocks and afterslip follow the same temporal evolution and that the spatiotemporal distribution of aftershocks is consistent with the idea that they are driven by reloading of the seismogenic zone resulting from frictional afterslip.

Citation: Perfettini, H., and J.-P. Avouac (2007), Modeling afterslip and aftershocks following the 1992 Landers earthquake, *J. Geophys. Res.*, *112*, B07409, doi:10.1029/2006JB004399.

1. Introduction

[2] Aftershocks and postseismic deformation are the most common manifestations of stress relaxation following large earthquakes. Relaxation can result from ductile deformation distributed within the lower crust and upper mantle [*Pollitz et al.*, 1998; *Deng et al.*, 1998], pore fluid flow [*Peltzer et al.*, 1998; *Bosl and Nur*, 2002], and localized shear due to ductile fault zone deformation or frictional sliding, hereafter referred to as afterslip. Afterslip can occur either updip or downdip of the ruptured zone [*Smith and Wyss*, 1968; *Marone et al.*, 1991; *Zweck et al.*, 2002; *Hsu et al.*, 2006]. Identifying the respective contributions of these various mechanisms is challenging, and the relation between aftershocks and postseismic deformation remains unclear. In some cases of large thrust events, it has been observed that aftershocks and geodetic deformation follow the same temporal evolution [*Perfettini and Avouac*, 2004a; *Perfettini et al.*, 2005; *Hsu et al.*, 2006]. This observation seems to hold also for the M_w7.3, 1992 Landers strike-slip earthquake (Figure 1). Indeed, we observe that the cumulative number of aftershocks with $M_w > 2$ within about 15 km of the ruptured faults [*Hauksson et al.*, 2003] follows the same time evolution as strain documented from near-field geodetic measurements (Figure 2) [*Savage and Svarc*, 1997]. The similarity between the two curves is unexpected if, as proposed by *Dieterich* [1994] and commonly accepted [e.g., *Stein*, 1999], aftershocks are driven by coseismic stress change with a delay determined only by the earthquake nucleation process. In the case of the Landers earthquake, Dieterich's model has been shown to provide a reasonable explanation of the temporal evolution and spatial distribution of aftershocks located more than 5 km away from the ruptured faults [*Gross and Kisslinger*, 1997]. However, it should be noted that the correlation in Figure 2 depends heavily on seismicity located less than 5 km away from the ruptured faults, which represent about 95% of the aftershocks [*Liu et al.*, 2003]. The correlation in Figure 2 therefore suggests that the time evolution of near-fault aftershocks and of postseismic deformation are linked.

[3] We begin by reviewing evidence for deep afterslip following the Landers earthquake (section 2), followed by our modeling approach (section 3). We then compare the predictions of our model with postseismic deformation (section 4) and with the spatial and temporal evolution of aftershocks (section 5).

2. Evidence for Deep Afterslip Following the Landers Earthquake

[4] Postseismic deformation following the M_w7.3, 1992 Landers earthquake was particularly well documented from geodetic measurements, including campaign GPS measurements by the U.S. Geological Survey (USGS), continuous GPS measurements by the Southern California Integrated GPS Network network (Figure 1) [*Shen et al.*, 1994; *Bock et al.*, 1997; *Savage and Svarc*, 1997; *Savage et al.*, 2003], and by synthetic aperture radar (SAR) interferometry [*Peltzer et al.*, 1996, 1998; *Massonnet et al.*, 1996; *Fialko*, 2004a]. To first order, GPS deformation follows approximately the

[1]Institut de Recherche pour le Développement/Observatoire Midi-Pyrénées, Toulouse, France.
[2]Tectonics Observatory, Division of Geological and Planetary Sciences, California Institute of Technology, Pasadena, California, USA.

0148-0227/07/2006JB004399$09.00

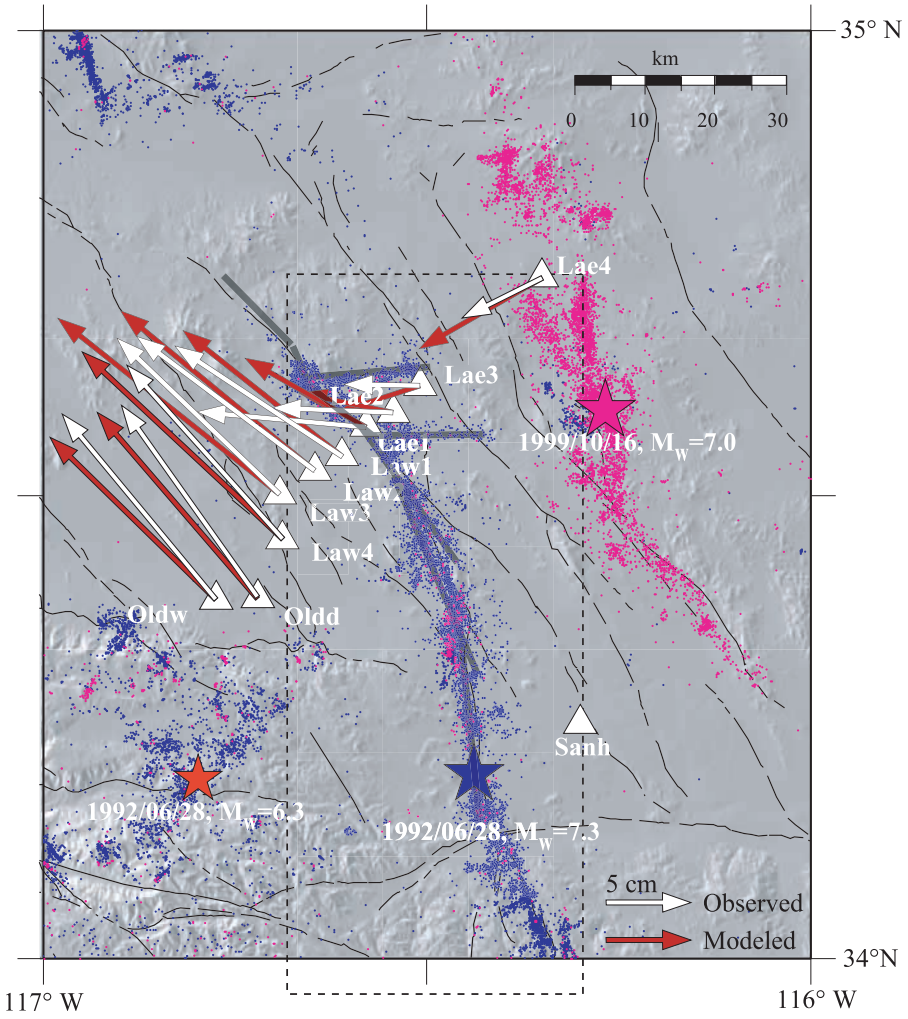

Figure 1. Map of the Landers area showing the M_w7.3 Landers epicenter (blue star) and its aftershocks (blue dots, pre-Hector Mine seismicity; pink dots, post-Hector Mine seismicity), the M_w7.1 Hector Mine epicenter (pink star), and the M_w6.5 Big Bear epicenter (red star). The white vectors show 6 years of postseismic surface displacements determined by the USGS from GPS campaign measurements (white triangles) relative to GPS station Sanh [*Savage and Svarc*, 1997; *Savage et al.*, 2003]. The red vectors show the corresponding displacements computed from our model. The region inside the dashed line is the zone used to represent the temporal evolution of seismicity in Figure 2 considering only the events with magnitude >2, hence larger than the detection threshold [*Hauksson et al.*, 2003]. The grey transparent lines show the simplified fault geometry of *Fialko* [2004b] used in this study.

same time evolution as aftershocks (Figure 2). It has been found that the near-field GPS measurements require some component of postseismic strain localized below the ruptured fault segments [*Savage et al.*, 2003; *Fialko*, 2004a]. Interferometric SAR (InSAR) measurements covering the period between the 1992 Landers and the 1999 Hector Mine earthquakes show that the dominant signal is due not only to poroelastic effects but also to near-fault displacement gradients, suggesting a relatively localized zone of postseismic deformation [*Peltzer et al.*, 1996, 1998]. The InSAR measurements, in fact, show a very limited effect of viscous relaxation over this time period [*Fialko*, 2004a]. The most plausible model satisfying all the data involves a combination of afterslip at depths greater than 10–15 km (mostly below the ruptured fault zone determined from the inversion of the near-field GPS data) and poroelastic deformation of the elastobrittle crust [*Savage and Svarc*, 1997; *Fialko*, 2004a]. No evidence for shallow afterslip was found in this particular case.

[5] In theory, postseismic deformation at midcrustal to lower crustal depths could reflect either viscous-like flow, distributed widely or localized within a ductile shear zone below the seismic fault zone, or brittle creep, a deformation process equivalent to rate-strengthening friction [*Hearn et al.*, 2002; *Montési*, 2004; *Fialko*, 2004a; *Savage et al.*, 2005; *Langbein et al.*, 2006]. We use here the term 'brittle creep' to refer to creep that occurs in the brittle domain as a result of intergrain frictional sliding and subcritical crack growth [*Scholz*, 1968; *Cruden*, 1970; *Cocks and Ponter*, 1989; *Amitrano and Helmstetter*, 2006]. This model of deformation, if distributed within a fault gouge zone, might also be called cataclastic flow. In laboratory experiments, brittle creep differs from ductile flow (due to intracrystalline dislocation creep or diffusion creep) in that the deformation

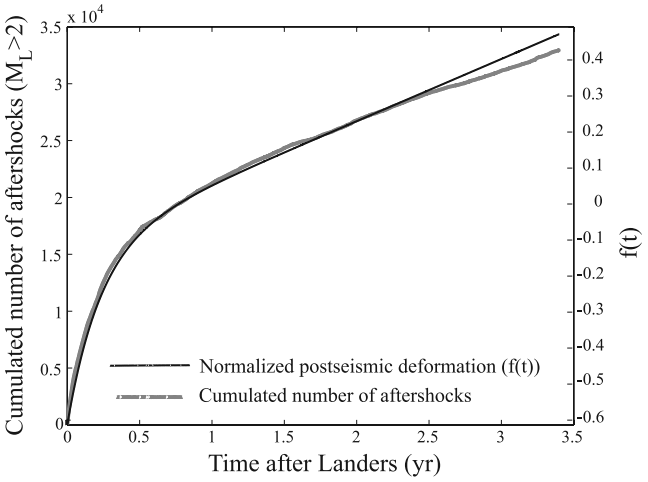

Figure 2. Cumulative aftershocks with $M_L > 2$ in the near-fault zone area outlined in Figure 1 and postseismic deformation as a function of time. Postseismic deformation is represented by the normalized function $f(t)$ characterizing the temporal evolution of surface displacements deduced from the principal component analysis of GPS times series [*Savage and Svarc*, 1997].

rate for brittle creep, instead of being a power law function, is some exponential function of the driving stress [*Lockner*, 1998]. This mechanism leads approximately to a 1/time decay of postseismic velocity [*Marone et al.*, 1991; *Perfettini and Avouac*, 2004a]. In a number of case studies of postseismic deformation, including the 1999 Izmit earthquake [*Hearn et al.*, 2002], the 1999 Chi-Chi earthquake [*Perfettini and Avouac*, 2004a; *Hsu et al.*, 2002; *Savage et al.*, 2005], the 2003 Tokachi-oki earthquake [*Miyazaki et al.*, 2004], and the 2005 Nias earthquake [*Hsu et al.*, 2006], the temporal evolution of afterslip was found to be consistent with brittle creep. From these observations it follows that as temperature increases with depth, fault friction changes from dominantly rate weakening at shallow levels, allowing for stick-slip behavior in the seismogenic fault zone (SFZ), to rate strengthening at greater depths, implying continuous creep [*Rice and Gu*, 1983; *Scholz*, 2002; *Marone*, 1998; *Blanpied et al.*, 1995]. The depth of the transition between these two behaviors is generally thought to correspond to the 250°C isotherm [*Blanpied et al.*, 1995], which is reached at a depth of about 15 km in southern California [*Lachenbruch and Sass*, 1973]. The area below the SFZ, which is presumably dominated by a rate-strengthening brittle rheology, is termed here, as in our previous studies, the brittle creep fault zone (BCFZ). In reality, the transition from rate weakening to rate strengthening depends not only on depth and temperature, but also on other factors, particularly lithology and fluids, which may be sources of spatial heterogeneities such that patches of crust with rate-weakening and rate-strengthening behavior might in fact interfinger.

3. Modeling Afterslip

3.1. Principle of the Modeling

[6] We assume here that afterslip following the Landers earthquake resulted from brittle creep, and estimate the rheological parameters required to fit the geodetic observations. For simplicity, we will assume that brittle creep is localized on a fault obeying a pure velocity-strengthening (VS) rheology (see Appendix A for a comparison with rate-and-state (RS) friction):

$$\tau = \tau_* + a\sigma \ln\left(\frac{V}{V_*}\right),\ a > 0 \tag{1}$$

where τ and σ are the shear stress and the effective normal stress, respectively, acting on the BCFZ, and V_* is a reference slip rate. The frictional parameters are the frictional stress $\tau_* = \sigma\mu_*$ at the reference velocity V_*, and $a\sigma$, which characterizes the dependency of friction on the slip rate and determines the dynamical response of the BCFZ to stress changes. We show in Appendix A that assigning a rate-and-state (RS) friction law to the BCFZ yields the same prediction except for a transient phase of probably too short duration to be detectable from the geodetic data available for the Landers earthquake. Note that in reality, creep could be distributed in a fault gouge zone of finite width, with the bulk rheology of the gouge obeying brittle creep (see *Perfettini and Avouac* [2004a] for discussion). According to (1), the friction coefficient τ/σ is a linear function of $\ln(V/V_*)$ with slope $a\sigma$.

[7] In previous investigations of fault zone rheology, one approach has been to invert the geodetic data for the slip history on the fault and to compute the varying shear and normal stresses during postseismic relaxation [*Miyazaki et al.*, 2004]. This approach does not take advantage of the fact that the coseismic stress change can be assessed. Also, the time evolution of slip is highly dependent on the parameters of the inversion. Here, we use a different approach by predicting the time evolution of afterslip from a forward dynamical model. A similar approach, adopted by *Hearn et al.* [2002] to model postseismic deformation following the 1999 Izmit earthquake, considers a finite element model. Here, we use instead an analytical formulation based on the theory of dislocations embedded in an elastic half-space [*Okada*, 1992]. The model is simple enough that it can be inverted for the frictional parameters. Given that the signature of afterslip is mainly seen in the near field GPS measurements by the USGS [*Savage and Svarc*, 1997; *Fialko*, 2004a] we will use only these data in our inversion. Thus we neglect possible trade-offs with other relaxation mechanisms.

3.2. Numerical Implementation

[8] We use the fault geometry (Figure 1) and coseismic slip distribution (Figure 3) obtained by *Fialko* [2004b]. The fault model consists of 357 rectangular fault segments extending vertically from the surface to a depth of 15 km. We assume that afterslip occurred on a fault zone along the downdip continuation of the ruptured faults, say at depth $z_0 = 15$ km, and resulted from the frictional response of the BCFZ to the coseismic stress change. The BCFZ extends vertically from z_0 to $z_0 + W_{bcfz}$, where W_{bcfz} is the downdip extent of the BCFZ and is discretized into $n_d = W_{bcfz}/dw$ cells along depth, and $n_s = L_{bcfz}/dl$ cells along strike. Here, L_{bcfz} is the total along-strike length of the fault segments of Fialko's model (grey transparent lines of Figure 1), and dl = 3 km and dw = 2.5 km. In reality, it is probable that

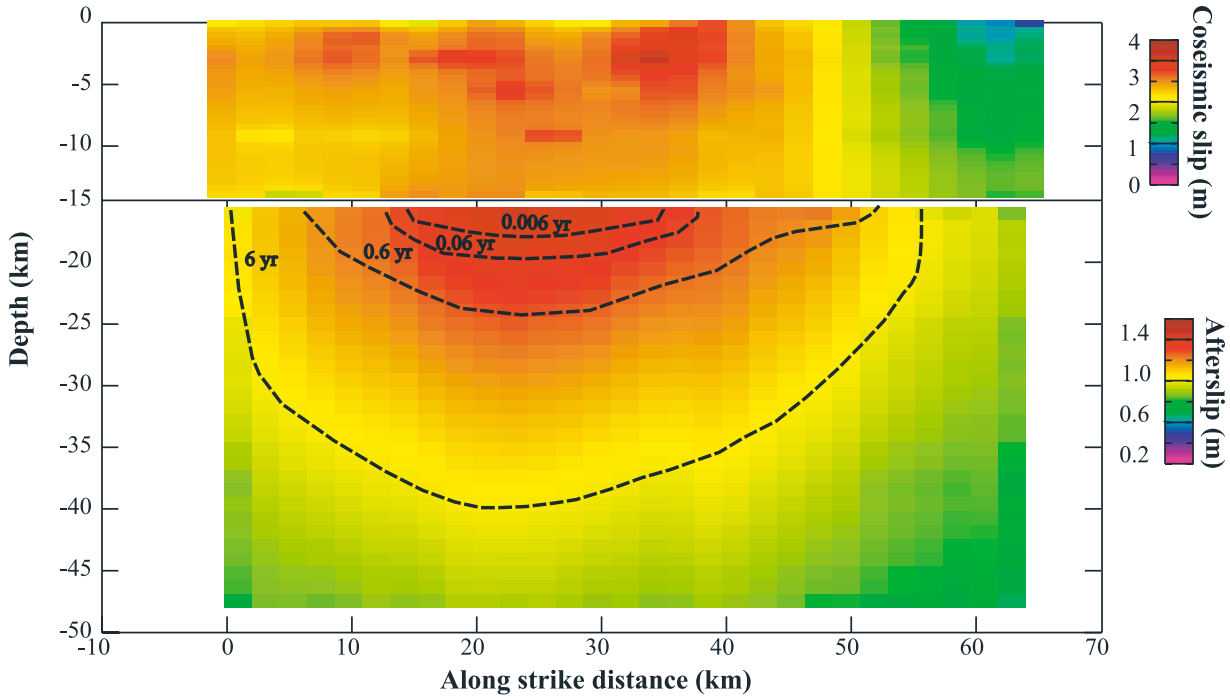

Figure 3. (top) Coseismic slip and (bottom) modeled postseismic slip after 6 years of relaxation. The time evolution of afterslip is represented by isochrons. Each isochron encompasses the zone within which the cumulative slip exceeds 70% of the peak slip at the considered time.

postseismic creep occurred at shallower depths than assumed here. Indeed, the creeping zone may overlap with the ruptured fault zone when seismic rupture propagates into the BCFZ [*Rice*, 1993]. The geodetic data do not provide enough constraints to resolve this issue.

[9] The balance of stresses computed in the center of cell i among the total number $n = n_s \times n_d$ of cells is

$$\tau(i,t) = \tau_0(i) + \Delta\tau_{el}(i,t) - \frac{G}{2\beta}V(i,t), i = 1,n, \qquad (2)$$

where $\tau_0(i)$ is the initial shear stress and $\Delta\tau_{el}(i, t)$ the shear stress changes induced by the evolution of slip on the BCFZ, assuming that the frictional resistance $\tau(i, t)$ of each cell i obeys the brittle creep rheology (equation (1))

$$\tau(i,t) = \sigma(i,t)\left[\mu*(i) + a(i)\ln\left(\frac{V(i,t)}{V*(i)}\right)\right], i = 1,n, \qquad (3)$$

where $\sigma(i)$ represents the effective normal stress on cell i. The parameters $\mu*(i)$ and $V*(i)$ are assumed to be spatially uniform. The static friction is set to a standard value of $\mu* = 0.6$ and corresponds to steady state sliding at the reference sliding velocity $V* = 10^{-6}$ m/s. These last two parameters have no effect on the dynamics of the system. The dimensionless parameter $a(i) > 0$ relates changes in the creeping rate to changes in the friction coefficient. The term $-(G/2\beta)V(i, t)$ is the radiation damping term, where G is the shear modulus set to 30 GPa, and β the shear wave velocity set to 3 km/s. Models considering this term are said to be quasi-dynamic because they incorporate the elastodynamic limit result for instantaneous changes of $V(i, t)$ [*Rice*, 1993]. This term, which is introduced to prevent infinite velocities from occurring in the simulations, is only active at large velocity ($\approx 2a\sigma\beta/G$ as further illustrated in equation (5)) and is effective only at early stages.

[10] The elastic shear stress changes induced by the evolution of slip on the BCFZ on cell i may be written

$$\Delta\tau_{el}(i,t) = \Sigma_{j=1}^{n} K(i,j)[\delta(j,t) - V_0 t], i = 1,n, \qquad (4)$$

where $\delta(j, t)$ is the displacement of cell j and V_0 the loading velocity. The component $K(i, j)$ of the elastic kernel represents the shear stress change induced by a unit slip on cell j in the rake direction of this cell computed in the direction of the rake of cell i, assuming a Poisson coefficient of $\nu = 0.25$ and a shear modulus of $G = 30$ GPa. Equation (4) is generalized to account for normal stress changes by substituting the Coulomb stress change ΔCFF [*Perfettini et al.*, 2003a] for $\Delta\tau_{el}$. The elastic kernels are computed using analytical solutions for stress and strain induced by a dislocation in an elastic half-space [*Okada*, 1992]. We neglect possible temporal variations in the rake, assuming that these are fixed by the coseismic stress change. We also consider that the constitutive parameters and effective normal stress do not vary with time ($da(i)/dt = d\mu*(i)/dt = 0$, $d\sigma(i)/dt = 0$) during postseismic relaxation.

[11] Combining equations (2), (3), and (4) yields, after derivation with respect to time,

$$\frac{dV(i,t)}{dt} = \frac{\Sigma_{j=1}^{n} K(i,j)[V(j,t) - V_0]}{\frac{\sigma(i)a(i)}{V(i,t)} + \frac{G}{2\beta}}, i = 1,n. \qquad (5)$$

Equations (4) and (5) implicitly assume that the BCFZ is embedded in a more extensive fault zone creeping at a

constant velocity V_0. Thus, when the BCFZ creeps at $V = V_0$, there is no elastic stress transfers and the regime is in steady state. This assumption is made in order to force the BCFZ to return to the steady state velocity V_0. It would be more realistic to take into account that the SFZ is probably locked in the interseismic period. The steady state regime should then correspond to a creep velocity tapering to zero at the top of the BCFZ. Our simplification implies that the preseismic velocity at the top of the SFZ is probably overestimated, and the braking effect due the relocking of the SFZ after the coseismic phase is underestimated. This assumption has no significant influence on the best fit models, as discussed in section 4.2.

[12] By combining equations (3) and (4), neglecting the radiation damping term and replacing the shear stress change $\Delta\tau_{el}(i, t)$ by the Coulomb stress change $\Delta\mathrm{CFF}_{stat}(i)$ $H(t)$, where $H(t)$ is the Heaviside function, we obtain an initial velocity distribution

$$V(i)^{+} = V(i)^{-} \exp\left[\frac{\Delta\mathrm{CFF}_{stat}(i)}{a(i)\sigma(i)}\right], i = 1, n, \qquad (6)$$

where $\Delta\mathrm{CFF}_{stat}(i)$ is the coseismic static Coulomb stress change computed using a coseismic slip model. V^{+} is the sliding velocity at the onset of postseismic relaxation, and V^{-} is the corresponding initial velocity. We make a distinction between V^{-} and V_0 because the nucleation process and the propagation of dynamic waves during the rupture process may contribute to accelerating creep within the BCFZ. It is also possible that due to coseismic stress transfer, the postseismic loading velocity resulting from viscous deformation at depth, characterized by V^{-}, is significantly larger than the preseismic loading velocity, characterized by V_0 [*Perfettini and Avouac*, 2004b; *Perfettini et al.*, 2005].

[13] To reduce the number of parameters of the model, we assume that the distribution of V^{-} is spatially homogeneous, such that $V(i)^{-} = V^{-}$ everywhere on the BCFZ. For simplicity's sake, we also assume homogeneous frictional properties, i.e., a constant value $a(i)\sigma(i) = a\sigma$. With these assumptions, the model depends only on four parameters: (1) V^{-}, the initial velocity; (2) $a\sigma$, a rheological parameter; (3) V_0, the loading velocity; and (4) W_{bcfz}, the downdip extent of the BCFZ.

[14] For any point $\mathbf{r} = (x, y, z)$ of the elastic medium, the displacement $U_i(\mathbf{r}, t)$ along the i axis resulting from slip on the BCFZ is computed from

$$U_i(\mathbf{r}, t) = \Sigma_{j=1}^{n} M_{i,j}(\mathbf{r}, t)\delta_j(t), \qquad (7)$$

where $M_{i,j}(\mathbf{r}, t)$ represents the displacement at $\mathbf{r}$ in the i direction induced by a slip unit on cell j in the direction of the rake of cell j. As for the matrix $K(i, j)$, $M_{i,j}$ is computed using elastic dislocations [*Okada*, 1992] with a Poisson coefficient of $\nu = 0.25$. Equation (7) states that in linear elasticity, the displacement $U_i(\mathbf{r}, t)$ of point $\mathbf{r}$ at any time t after the main shock results from the summation of the contributions of each individual slip $\delta_j(t)$ of each cell j of the BCFZ. In theory, the observed displacements result not only from transient creep on the BCFZ but also from interseismic deformation taking place elsewhere than on the BCFZ and not explicitly taken into account in our model. The model ignores in particular the effect of deep seated deformation below the BCFZ. The model also ignores the effect of interseismic loading on the fault segments which did not break during the Landers earthquake. We believe that those are reasonable assumptions given that the geodetic velocities over the 6 years of postseismic deformation analyzed here are at least one order of magnitude larger than what is expected from interseismic loading on the Landers fault zone. Indeed, the long-term slip rate across the Landers fault zone is estimated to be on the order of only tenths of mm/yr [*Rubin and Sieh*, 1997]. We discuss those assumptions more in detail in section 4.2.

4. Results of the Modeling of Afterslip

4.1. Determination of the Best Fitting Model

[15] A linear array of 10 GPS monuments, Oldw, Oldd, Lae4, Lae3, Lae2, Lae1, Law1, Law2, Law3, and Law4 (Figure 1), was installed by the USGS across the Emerson fault segment 12 days (0.034 year) after the Landers main shock. This array provided an exceptional record of postseismic deformation in the near field [*Savage and Svarc*, 1997; *Savage et al.*, 2003]. Following *Savage and Svarc* [1997], we model the relative displacement of these 10 stations relative to the GPS station Sanh (Figure 1), located about 40 km southeast of the transect (Figure 1). We verify a posteriori that the model predicts a reasonable fit to the displacement of Sanh relative to stable North America.

[16] We seek the set of parameters ($a\sigma$, V_0, V^{-}, W_{bcfz}) that minimizes the root-mean-square (RMS) between the modeled and observed postseismic displacements. The parameters' space was first explored using a genetic algorithm [*Goldberg*, 1989] and refined around the minimum using simulated annealing combined with the downhill simplex method of *Nelder and Mead* [1965] [see *Press et al.*, 1992]. The best fitting model corresponds to $V^{-} \approx 75$ mm/yr, $a\sigma \approx 0.49$ MPa, $W_{bcfz} \approx 85$ km, and $V_0 \approx 1.8$ mm/yr. This model yields a RMS of 12.2 mm (Figure 4) and falls into the range of the $1 - \sigma$ uncertainties on the geodetic measurements that are estimated to be on the order of 4–20 mm [*Savage et al.*, 2003]. We consider the fit to the data to be satisfactory, since the measurements appear to be randomly distributed around the predicted values. We see no systematics that would suggest that the model is inadequate or could be significantly improved. The model predicts a reasonable fit to the displacement of the reference station Sanh relative to stable North America (Figure 5), taking into account the effect of interseismic strain associated with the San Andreas fault system based on the work by *Gordon et al.* [1993]. The model also adjusts reasonably well the 1992–1999 displacements relative to North America measured at a number of regional sites by Southern California Earthquake Center (SCEC) and the USGS that were not included in the analysis (Figure 6).

4.2. Model Uncertainties, Trade-offs and Significance of the Model Parameters

[17] Because of various trade-offs among the model parameters, the best fitting model is in fact only marginally better than other, relatively different models. We have investigated these trade-offs and the uncertainties on the model

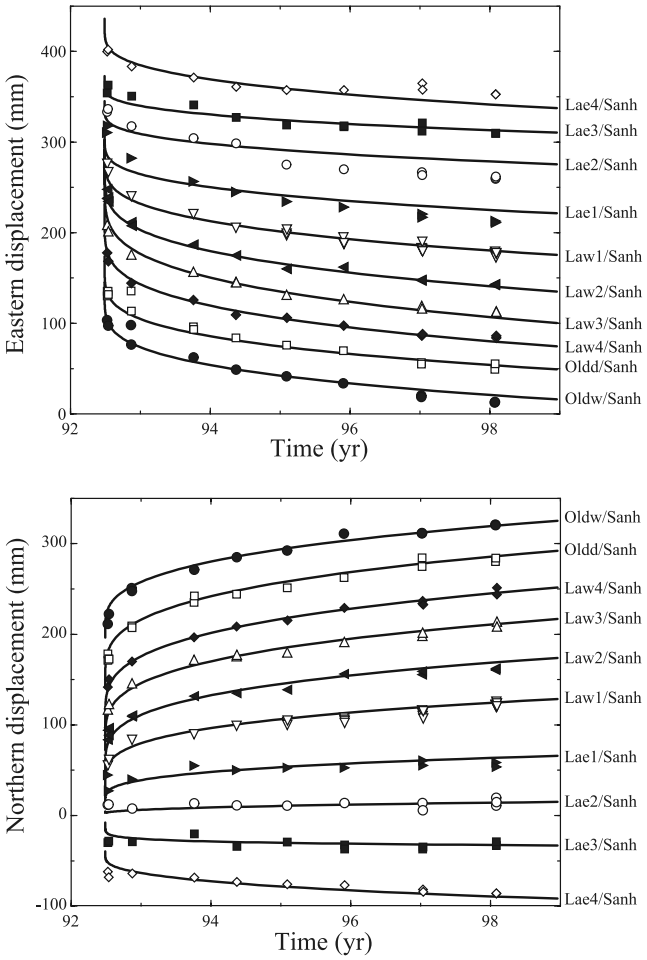

Figure 4. Observed [*Savage and Svarc*, 1997] and modeled postseismic displacements relative to station Sanh. The continuous line represents the predictions of the best fitting model, which corresponds to $V^- \approx 75$ mm/yr, $a\sigma \approx 0.49$ MPa, $W_{bcfz} \approx 85$ km, and $V_0 \approx 1.8$ mm/yr, yielding an RMS of 12.2 mm.

parameters by systematically exploring various models and selecting those acceptable at the 67% confidence level (Figure 7). To do so, we used chi-square statistics and rescaled the $1-\sigma$ uncertainty on the geodetic measurements to 12.2 mm so that the reduced chi-square is unity for our best fitting model.

[18] In Figure 7, we plotted the values of the parameters corresponding to the different models. At the 67% confidence level, $a\sigma$ is constrained to stand between 0.47 and 0.53 MPa, V_0 is any value lower than 19.5 mm/yr, V^- is constrained to between 53.5 and 98.4 mm/yr, and W_{bcfz} falls between 46.3 and 94.5 km. The preseismic loading velocity V_0 is poorly constrained, mostly because of a lack of preseismic geodetic data that could constrain the asymptotic behavior of the model.

[19] The most realistic models can be chosen based on considerations other than fit to the geodetic data. One such piece of information is the long-term geologic slip rate on the faults that ruptured during the Landers earthquake, which is estimated to be on the order of tenths of mm/yr [*Rubin and Sieh*, 1997]. A long-term slip rate of a few mm/yr at most is also required for the 7–12 mm/yr horizontal shear across the East California Shear Zone [*Sauber et al.*, 1986; *Savage et al.*, 1990; *Sauber et al.*, 1994]. We may then consider that only models with a loading velocity V_0 of less than a few mm/yr are acceptable. Our modeling then shows that the effective loading velocity V^- needs be much larger than V_0 (between 60 and 100 mm/yr), and $a\sigma$ needs to be in the upper range of possible values (0.48–0.53 MPa).

[20] The long-term velocity V_0 is only loosely constrained from the braking effect that this parameter introduces to the modeling. Indeed, over the time period covered by the data analyzed here, the creeping velocity is always much larger than the asymptotic value V_0. As mentioned earlier, equation (5) assumes that the BCFZ is embedded within a more extensive fault zone that slips at V_0 so that in our modeling, the braking effect of the relocking of the SFZ is underestimated. This is probably not an issue because the postseismic slip right below the SFZ exceeds 1 m over the 6 years modeled here. The postseismic slip is also several orders of magnitude larger than the implicitly assumed slip on the SFZ over the same period, which reaches a few centimeters at most even if a relatively large V_0 is allowed. The braking effect computed from our modeling does not differ significantly from that which would be obtained by assuming complete relocking of the SFZ during postseismic deformation. In fact, the sensitivity tests formally show that the distinction between V^- and V_0, is unnecessary. The model corresponding to $V^- = V_0 = 33.7$ mm/yr, $a\sigma = 0.45$ MPa, and $W_{bcfz} \approx 43.7$ km yields an RMS of 12.6 mm, which is nearly as good as the best fitting model obtained by allowing V^- to differ from V_0.

[21] The uncertainty in the model's parameters is also due in part to strong interdependencies. In particular, $a\sigma$ varies with V^- as expected from equation (6) (Figure 7d), given that all the models fitting the data must yield about the same V^+. We also see that V^- decreases with V_0 (Figure 7a), a result that is expected given that the higher the long-term velocity, the lower the initial velocity. The interplay between W_{bcfz} and the other parameters is weak. The sensitivity tests show that the only constraint on W_{bcfz} is that it must be larger than 45 km. This is simply a consequence of the fact that complete relaxation is not reached after the $t_{obs} = 6$ years of postseismic deformation analyzed here, so that all models implying a relaxation time significantly larger than t_{obs} are admissible (as long as they also share the same V^+). The relaxation time associated with brittle creep in a one-dimensional (1-D) model loaded at constant velocity V_{load} is $t_r = a\sigma/(KV_{load})$, where K is the stiffness of the fault [*Perfettini et al.*, 2005]. The equivalent stiffness in our model is $K = G/W_{bcfz}$, and the effective loading velocity is V^-, so the relaxation time can be estimated from

$$t_r = \frac{a\sigma W_{bcfz}}{GV^-}. \tag{8}$$

The acceptable models in Figure 7 all correspond to a relaxation time t_r larger than 10 years. For $V^- \approx 80$ mm/yr and $a\sigma \approx 5$ MPa we get that W_{bcfz} needs to be larger than 29 km for the relaxation time to be longer than t_{obs}. The width of the BCFZ may then be seen as a proxy for the relaxation time in a 1-D approximation. In other words, the larger the width of the fault zone, the longer it takes for

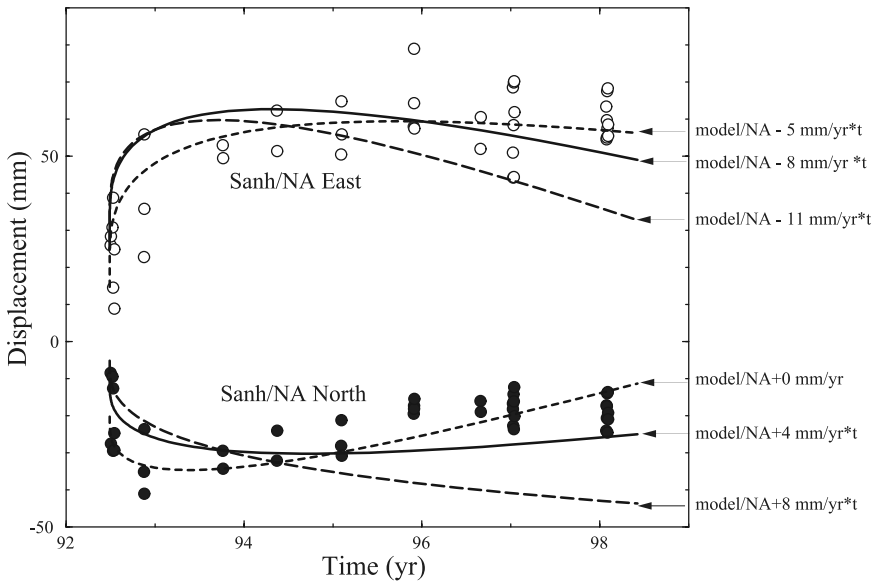

Figure 5. Measured and predicted horizontal displacements at site Sanh relative to stable North America. The contribution of the San Andreas fault system is taken into account using the model of *Gordon et al.* [1993], which predicts a long-term velocity at Sanh relative to North America of -8 ± 3 mm/yr eastward and 4 ± 4 mm/yr northward (solid lines). The dashed lines correspond to the most extreme velocities of *Gordon et al.* [1993].

postseismic slip to spread over the entire BCFZ, and the longer the relaxation process lasts.

[22] Despite the simplicity of the model and the limited number of free parameters, the modeling provides a good fit to the available geodetic observations. The best constrained parameters in this modeling are thus $a\sigma$ (0.48–0.53 MPa) and V^- (60–100 mm/yr). The BCFZ alone contributes to most of the observed postseismic slip because of the large value of V^- (compared to V_0) determined in our best fit models (Figure 7). The fact that V^- greatly exceeds V_0 over such a large region suggests that the effective loading velocity of the BCFZ is V^- rather than V_0, as implicitly assumed in the estimate of the relaxation time (see equation (8)). Indeed, substituting V^- for V_0 in equation (5) leads to fits nearly indistinguishable from the solutions obtained when V_0 is kept. In addition, the long-term velocities observed in Figure 4 at the end of the observation period corresponds to the entire BCFZ creeping at the velocity V^-, reinforcing its interpretation in terms of an effective loading velocity. Although poorly constrained, V_0 plays an important role in the model in that it introduces a braking effect on postseismic creep and allows the asymptotic behavior of the model to be consistent with the low geological rate of motion across the Landers fault zone.

[23] In section 4.3 we discuss the significance of the depth range of the BCFZ and the large effective loading velocity V^-.

4.3. Significance of Deep Afterslip and Large V^-

[24] The inferred width of the BCFZ, between 46–93 km, is probably not very meaningful. Indeed, only the upper few kilometers of the BCFZ plays an important role in the relaxation process during the first few years following the main shock (Figure 3). Most of the early afterslip occurs at the top of the BCFZ, and afterslip at greater depths is modeled from a frictional law, although a viscous flow law would probably be more appropriate at these depths. It is therefore probable that the model mimics, in part, the effect of a viscous shear zone at depth by frictional afterslip, and this might bias our estimate of the rheological parameters.

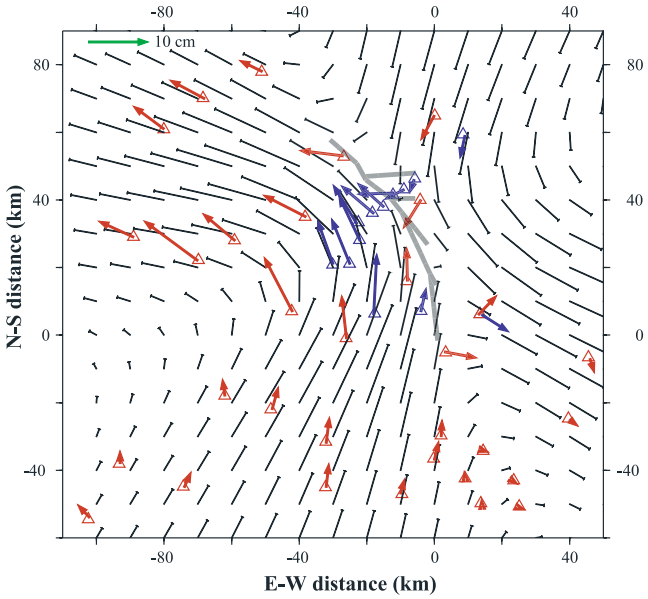

Figure 6. Postseismic horizontal displacements from 1992 to 1999 relative to stable North America. Measurements from the USGS (blue symbols) [*Savage and Svarc*, 1997] were used in the inversion and the SCEC data (SOPAC: http://sopac.ucsd.edu/dataArchive/) (red symbols) were not. Black arrows show the velocities predicted by our model. Thick lines show the simplified fault geometry [*Fialko*, 2004b] used in this study.

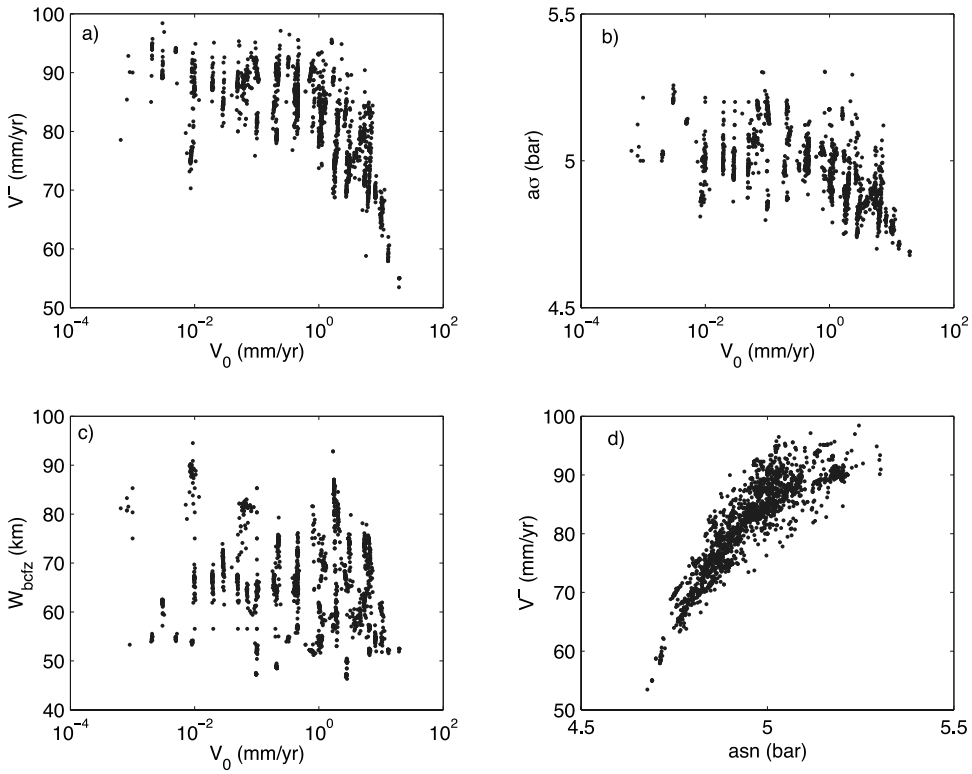

Figure 7. Values of model parameters acceptable at the 67% confidence level. In this plot, we have selected all models yielding a fit to the measurements better than 12.34 mm/yr (corresponding to a reduced chi-square of 1). (a) Initial velocity V^- as a function of long-term loading velocity V_0. (b) Rheological parameter $a\sigma$ as a function of V_0. (c) Width W_{bcfz} of the BCFZ as a function of V_0. (d) V^- as a function of $a\sigma$.

In Appendix B, we show that the velocity-strengthening rheology used here is equivalent to a linear viscous rheology in the limit of small stress changes (compared to $a\sigma$). The deep postseismic creep in our model could, for example, stand for viscous flow within a kilometer-scale wide shear zone with a viscosity of about 10^{19} Pa s. The fact that our model is able to mimic not only the early response but also the long-term behavior of deformation suggests that this approximation is probably valid.

[25] A striking feature of the modeling presented here is that it requires a fairly large effective loading velocity V^-, in the range of 60–100 mm/yr. One possible explanation is that the model assumes a velocity-strengthening (VS) friction law rather than a rate-and-state (RS) friction law. It is shown in Appendix A that those two laws lead to different predictions in the early phase of postseismic relaxation namely for times $t < t^* = d_c/V_1$ where V_1, given by equation (A5), is the initial velocity in the RS case. At later times, both laws lead to an identical response providing that the assumed initial velocity at the onset of postseismic slip in the VS case is equal to the velocity V_2 (see equation (A6)) at the end of the transient phase in the RS case. Therefore, for the two models to be equivalent at time $t \gtrsim t^*$, the initial velocity V_2 in the VS case needs to be larger than V_1 in the RS case. In the example shown in the Appendix A this ratio is 40 but could be arbitrarily large as a/b approaches 1 because according to (6), V_2 becomes unbounded as $a \rightarrow b^-$.

[26] Another possible explanation for this might be that the coseismic stress increase on the creeping fault zone is underestimated because of the assumed depth range of the BCFZ. Namely, it might be argued that postseismic slip occurs much shallower than the 15 km depth assumed here. We have tested various depths for the upper edge of the BCFZ between 15 and 0 km and noticed that the value only marginally affects the modeling results. In all cases, we found that V^- must be on the order of tens of mm/yr, always too large to be assumed equal to V_0, and to extend to rather great depths.

[27] Another reason that V^- is large is that creeping velocities can increase due to the dynamic stresses generated by the main shock to more than what is estimated in the modeling, which only takes into account the static stress change. This mechanism probably occurs in nature, as demonstrated from the observation that shallow surface fault creep can be accelerated by distant earthquakes [*Hudnut and Clark*, 1989; *Bodin et al.*, 1994; *Amelung and Bell*, 2003] or that landsliding can be accelerated by seismic waves generated by nuclear tests [*Bouchez et al.*, 1996]. If a standard velocity-strengthening or rate-and-state rheology is assumed, such an acceleration would not take place due to the short duration of the seismic wave train [*Perfettini et al.*, 2003b]. Acceleration of creep by seismic waves might in fact occur in the presence of fluids released during fault gouge overpressurization.

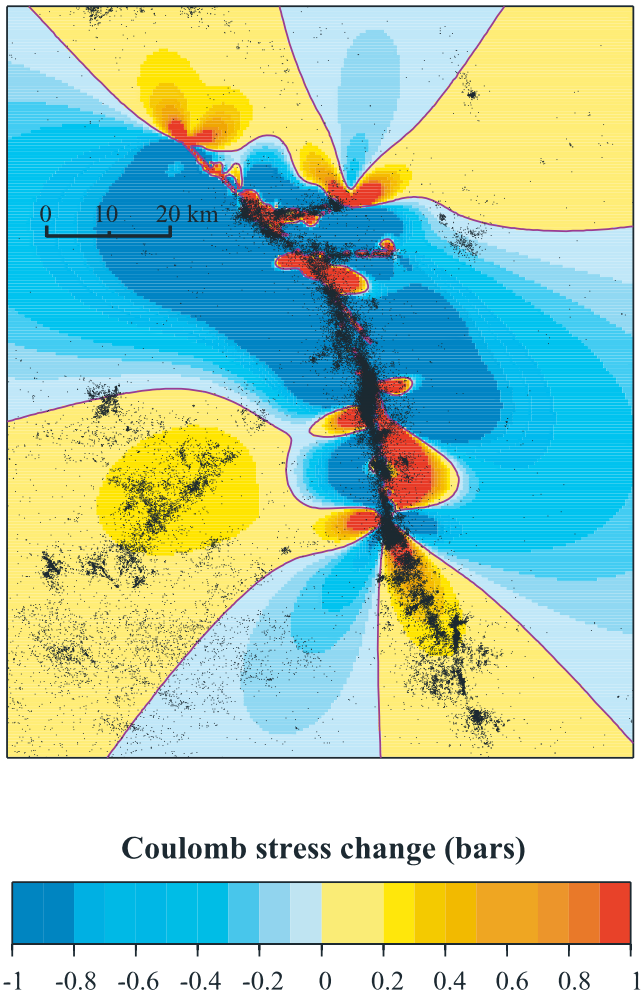

Figure 8. Coseismic Coulomb stress changes induced by the Landers main shock computed at 10 km on right-lateral receiver faults striking N340°E.

[28] It is also possible that the BCFZ could have accelerated in the preseismic phase due to the occurrence of a slow slip transient, a mechanism that may promote the nucleation of subduction earthquakes [e.g., *Dragert et al.*, 2001]. This speculative scenario is not testable with the available geodetic data.

[29] Given the exponential dependence of the slip rate on $a\sigma$ a factor of 50 increase in V^+ could be achieved with just a several percent reduction in $a\sigma$. *Blanpied et al.* [1995] have shown experimentally a linear increase with temperature of the $a_{RS} - b_{RS}$ parameter defined in equation (A3). On the basis of the correspondence between the RS and VS rheologies discussed in Appendix A, this experimental result suggests that in our model the parameter a may increase with temperature and hence depth. The effective normal stress σ is also expected to increase with depth as does the lithostatic stress. Equation (6) shows that even a small increase of $a\sigma$ with depth would imply a much larger response of the shallower part of the BCFZ than the deeper one, this feature being enhanced by the expected decay of coseismic stress changes with depth. So it is possible that the large value of V^- needed in the model simply reflects a moderate increase of $a\sigma$ with depth.

[30] A final alternative scenario that could lead to a large V^- is a loading velocity due to viscous deformation that is much higher in the early postseismic phase than is the long-term geological rate estimated across the Landers fault zone. This mechanism is possible if the coseismic stress change at depth, where viscous flow is dominant, is large compared to the average shear stress driving viscous deformation in the interseismic period [*Perfettini and Avouac*, 2004b]. From modeling the viscoelastic response of the lithosphere, *Pollitz et al.* [2000] has shown that viscous deformation at depth could have accelerated by a factor of ~3 as a result of the static coseismic stress change associated with the Landers earthquake. However, we believe that this effect alone is insufficient to explain the large value of V^- estimated from our modeling.

5. Relationship Between Postseismic Deformation and Aftershocks

5.1. Principle of the Analysis

[31] In this section, we compare the spatiotemporal distribution of seismicity to the stress changes induced by either coseismic deformation or by postseismic relaxation. To assess postseismic stress variations we use the afterslip model that fits best the geodetic data described in section 4.

[32] For this comparison, we make the common assumption that earthquakes are triggered where the medium is locally brought closer to failure. We assume a Mohr-Coulomb failure criterion so that failure is promoted where the Coulomb stress, ΔCFF, increases, and vice versa [e.g., *King et al.*, 1994; *Stein*, 1999]. The Coulomb stress change at a given site $\mathbf{r}$ is defined as $\Delta\mathrm{CFF}(\mathbf{r}; t) = \Delta\tau(\mathbf{r}; t) + \mu_0\Delta\sigma(\mathbf{r}; t)$, where μ_0, assumed equal to 0.6, is the coefficient of friction of the receiver fault, $\Delta\tau(\mathbf{r}; t)$ and $\Delta\sigma(\mathbf{r}; t)$ are the changes in shear and effective normal stresses, respectively, induced at point $\mathbf{r}$ by afterslip (and defined as negative in compression).

[33] We compute the Coulomb stress changes on vertical faults striking parallel to the mean strike, N340°E, of the Landers fault ruptures. The Coulomb stress on faults with this strike is nearly maximum, as shown from the stress field deduced from the focal mechanisms of local earthquakes recorded either before or after the Landers earthquake [*Hardebeck and Hauksson*, 2001]. This approach is approximately equivalent to computing the Coulomb stress change on faults whose orientations are optimal with respect to the regional stress field, given that the principal regional stress did not rotate by more than 15° during postseismic relaxation [*Hardebeck and Hauksson*, 2001].

[34] An alternative approach would have been to evaluate the Coulomb stress change on fault planes optimally oriented with respect to the local postseismic stress field, itself computed accounting for modeled coseismic and postseismic deformation. This would enhance the zones with increased Coulomb stress due either to coseismic or to postseismic deformation. The effect would be most significant for the coseismic Coulomb stress change in the near field area, where modeled coseismic stress changes are large. The corresponding results are highly dependent on the

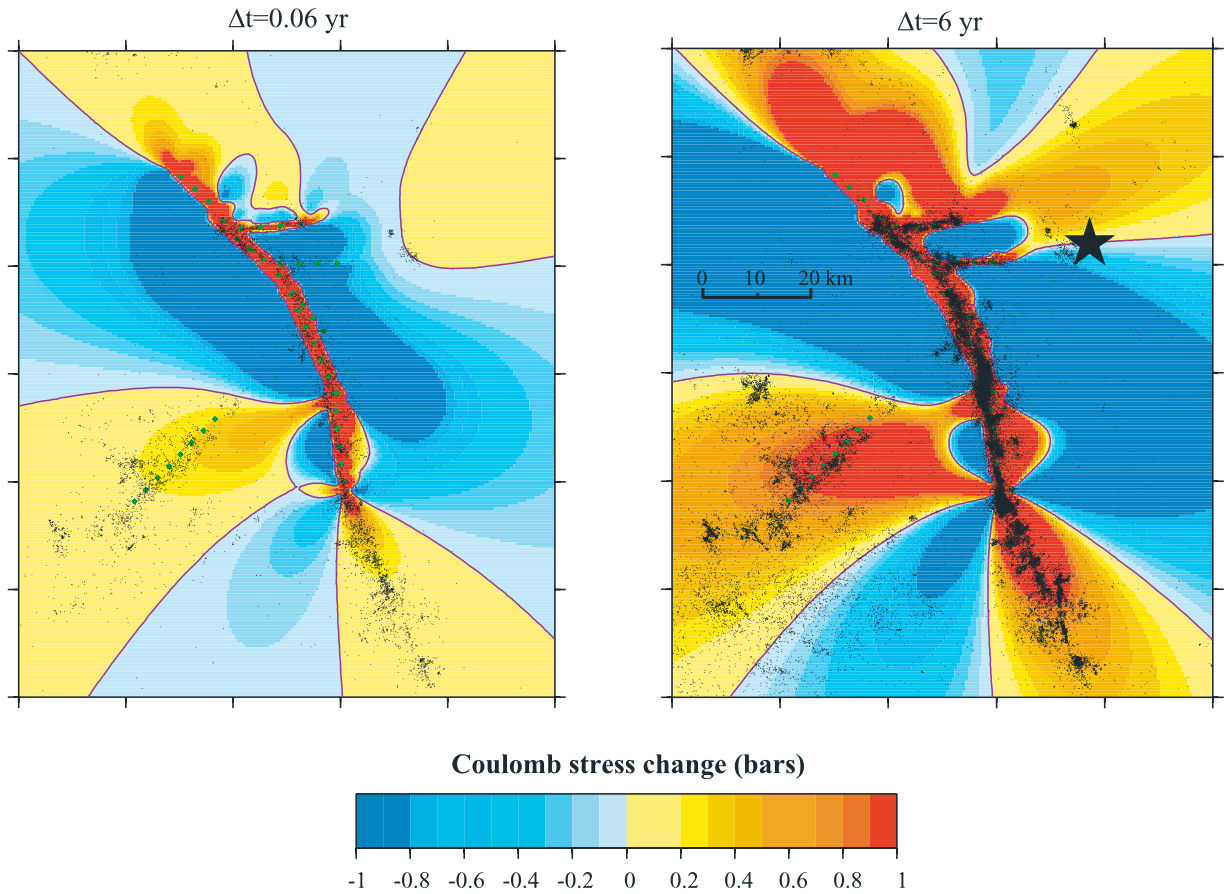

Figure 9. Coulomb stress changes computed at the bottom of the seismogenic fault zone. The maps shows Coulomb stress changes on right-lateral faults striking N340°E computed at the top of the brittle creep fault zone, somewhat arbitrarily set to 15 km depth, induced by (left) 0.06 year and (right) 6 years of afterslip. Aftershocks with $M_L > 2$ over the same time period are also shown for comparison. See Figure 12 for cross sections.

coseismic slip model and partly biased by the singularity of Okada's analytical expression as one gets close to the elastic dislocations. On the basis of the analysis of *Hardebeck and Hauksson* [2001], we can exclude that the aftershocks occurred in areas where the stress field was significantly altered by coseismic deformation. We therefore prefer to neglect the effect of coseismic deformation on the orientation of the stress tensor.

5.2. Spatial Correlation

[35] Figure 8 shows the coseismic Coulomb stress changes computed at a depth of 10 km onto right-lateral faults striking N340°E. The pattern of Coulomb stress change, ΔCFF, induced by coseismic deformation (Figure 8) and by afterslip (Figures 9 and 10) turns out to be quite similar away from the fault zone, in areas of increased Coulomb stress where most aftershocks occur. They differ most significantly in the near-fault zone, where ΔCFF induced by slip on the BCFZ is maximum and systematically positive, while coseismic deformation shows a complex pattern with spots of decreased Coulomb stress (Figure 8). Given that the assumed coseismic slip distribution is relatively smooth, the dominant pattern of coseismic Coulomb stress change is a decrease in the near-fault zone. In reality, the slip distribution is probably more heterogeneous than assumed in the model, so that there would be areas of increased Coulomb stress in the near field. In practice, static coseismic Coulomb stress changes in the near field cannot be reliably estimated due not only to uncertainties in the details of fault geometry and slip distribution [*King et al.*, 1994] but also to singularities of Okada's equations close to the modeled dislocations [*Okada*, 1992]. This is why the near-fault domain is generally not considered in studies of the relationship between aftershocks and coseismic Coulomb stress change [*Gross and Kisslinger*, 1997; *Hardebeck et al.*, 1998], even though most aftershocks occur there. In the case of the Landers earthquake, about 95% of the aftershocks occurred within 5 km from the faults ruptured during the main shock [*Liu et al.*, 2003].

[36] Afterslip tends to further increase the Coulomb stress changes in areas already brought closer to rupture during the main shock both in the immediate vicinity of the faults ruptured during the main shock and farther away. Vertical Coulomb cross sections along the lines of Figure 11 are shown in Figure 12. The spatial correlation between increased Coulomb stress due to afterslip and seismicity is quite good also in the near field, as illustrated by Figure 12. To better illustrate the agreement between the spatial distribution of aftershocks and Coulomb stress changes, we estimate the cumulative number $N_{\mathrm{cum}}(i)$ of aftershocks in

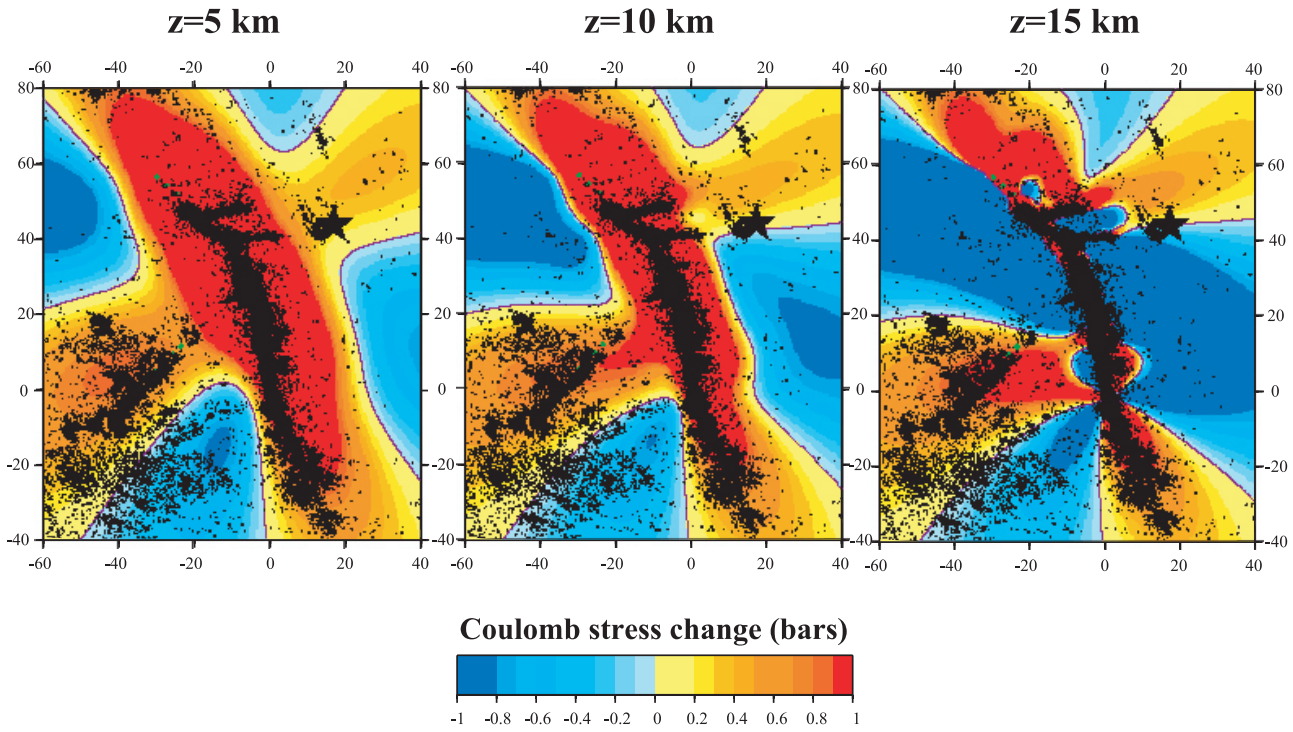

Figure 10. Map of Coulomb stress changes computed at depths of 5, 10, and 15 km on right-lateral receiver faults striking N340°E.

each cell i of size 1 km × 1 km. All of the aftershocks with $M_L > 2$ occurring over the first 6 years following the Landers earthquakes are considered. If our computation predicts an increase in Coulomb stress in cell i, the cumulative number of aftershocks is plotted in red. If the predicted Coulomb stress is negative, then $-N_{cum}(i)$ is plotted in blue. The corresponding results are shown in Figure 13 considering postseismic Coulomb stress changes and Figure 14 considering coseismic Coulomb stress changes. Table 1 shows the percentage of events consistent with the pattern of coseismic and postseismic deformation at various depths (z = 5, 10, and 15 km). At least 90% of the aftershocks are located in areas of increased postseismic Coulomb stress, while at most, 60% of them are located in areas of increased coseismic Coulomb stress. The discrepancy between the two models comes essentially from aftershocks near the ruptured fault where the coseismic model is probably not accurate enough for this correlation to be meaningful. By varying the depth of the upper edge of the creeping zone we have found that the agreement between the increased Coulomb stress due to afterslip and the spatial distribution of aftershocks can be improved if this depth is assumed to be shallower, for example, around z_0 = 12 km rather than 15 km. It is highly probable that the depth of the BCFZ is variable and may overlap with the seismogenic fault zone, as is suggested by some case studies of natural examples [e.g., *Hsu et al.*, 2002] and by theoretical considerations [*Rice*, 1993; *Lapusta and Rice*, 2003]. The geodetic data available for the Landers earthquake are, unfortunately, insufficient to address that point.

5.3. Temporal Correlation

[37] If we assume, as a first-order approximation, that the seismicity rate $R(\mathbf{r}, t)$ at a given time t and at a given point $\mathbf{r}$ of the medium is proportional to the Coulomb stress rate $d\Delta\mathrm{CFF}(\mathbf{r}; t)/dt$ at this given point, we obtain

$$R(\mathbf{r},t) = \alpha(\mathbf{r})\frac{d\Delta\mathrm{CFF}(\mathbf{r};t)}{dt}, \tag{9}$$

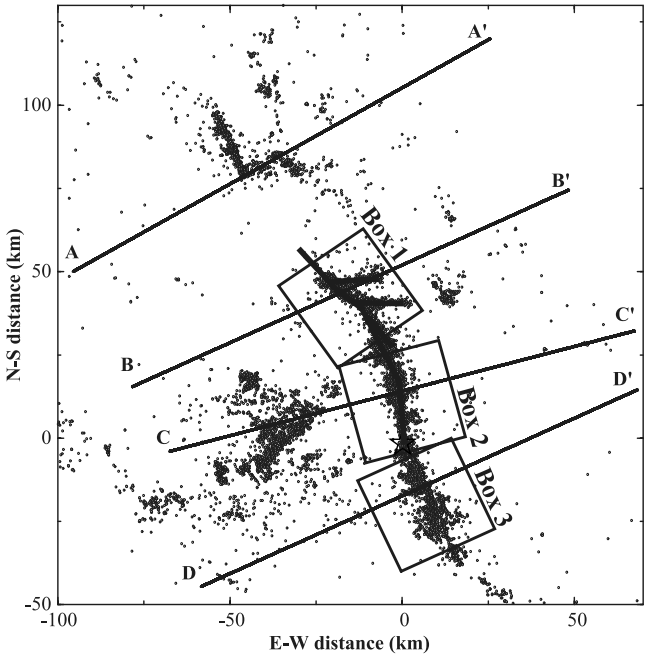

Figure 11. Locations of lines AA′, BB′, CC′, and DD′, along cross sections of Figure 12. Also shown are the locations of the boxes used to plot Figure 15.

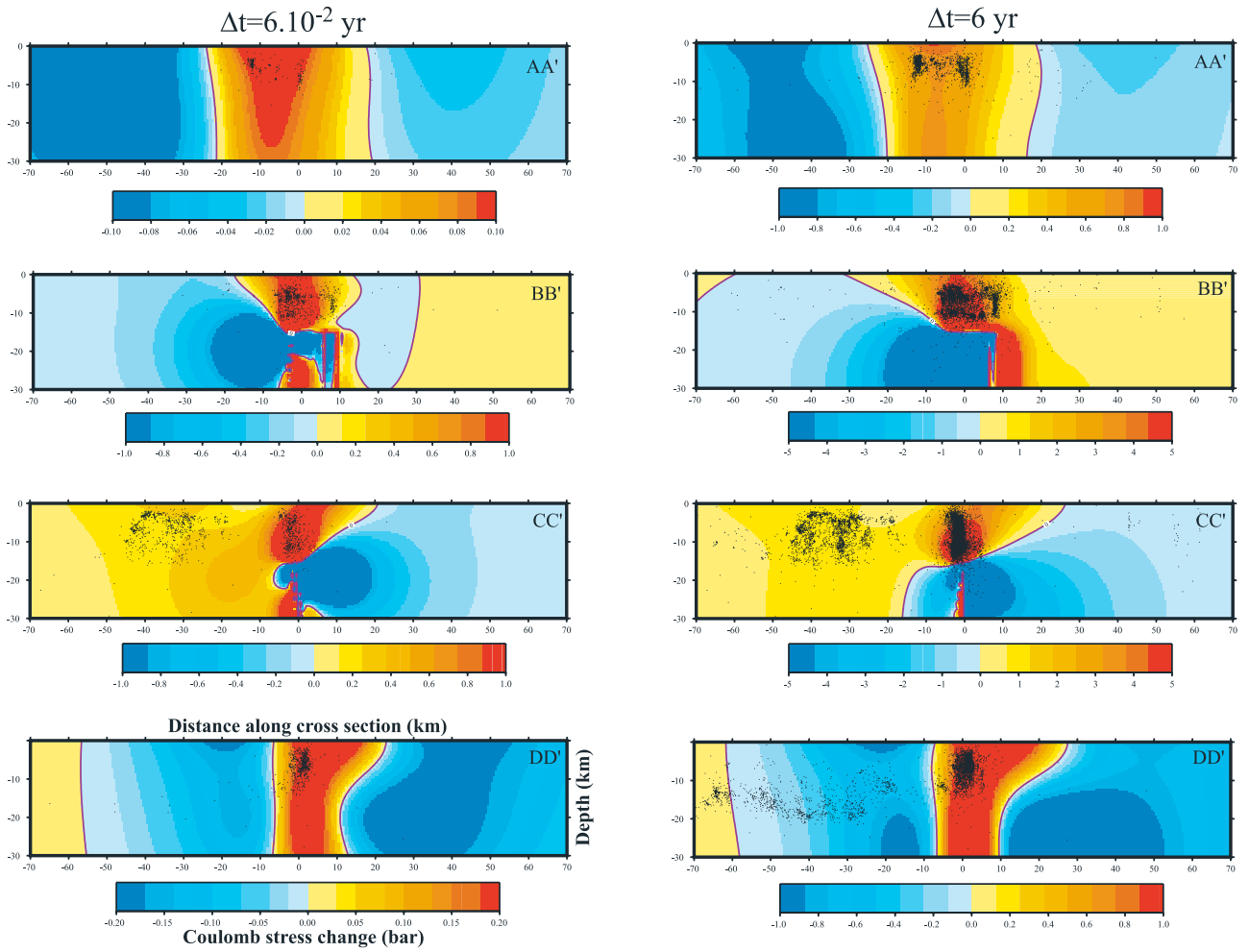

Figure 12. Cross sections of Coulomb stress changes induced by afterslip along the profiles AA′, BB′, CC′, and DD′ of Figure 11 at (left) 6×10^{-2} years after the main shock and (right) 6 years after the main shock.

where the constant of proportionality α characterizes the potential of the medium at point $\mathbf{r}$ to produce seismicity in response to a given Coulomb stress change. It is expected to depend on the density of faulting and on mechanical properties that are assumed to be independent of time. The cumulative number of earthquakes $N(\mathbf{r}, t)$, is obtained by integrating equation (9) with respect to time

$$N(\mathbf{r},t) = N(0) + \alpha(\mathbf{r})[\Delta\mathrm{CFF}(\mathbf{r};t) - \Delta\mathrm{CFF}(\mathbf{r};0)], \qquad (10)$$

where $N(0)$ is the cumulative number of earthquakes at time $t = 0$, and $\Delta\mathrm{CFF}(\mathbf{r}; 0) = 0$ since, immediately after the main shock, the BCFZ has not yet started to load the surrounding medium. Let $t_{\max}$ be the total duration of the considered period, which ends in October 1999, at the time of the Hector Mine earthquake. We use here the rounded value $t_{\max} = 6$ years. The normalized cumulative number of earthquakes is then written as

$$\overline{N}(\mathbf{r},t) = \frac{N(\mathbf{r},t) - N(0)}{N(\mathbf{r},t_{\max}) - N(0)}, \qquad (11)$$

and the normalized Coulomb stress change is given by

$$\overline{\Delta\mathrm{CFF}}(\mathbf{r};t) = \frac{\Delta\mathrm{CFF}(\mathbf{r};t)}{\Delta\mathrm{CFF}(\mathbf{r};t_{\max})}. \qquad (12)$$

Equation (10) is then simply

$$\overline{N}(\mathbf{r},t) = \overline{\Delta\mathrm{CFF}}(\mathbf{r};t). \qquad (13)$$

This normalization requires all curves to start and end at the same point.

[38] Figure 15 shows the temporal evolution of the normalized cumulative number of aftershocks whose epicenters are located within the boxes of Figure 11. Normalized Coulomb stress changes are also shown and are computed at $z = 15$ km (near their maximum values) at the center of the same boxes. The correlation between the two curves is strongest in box 2, which is the area with maximum afterslip in our model. In box 1 the correlation is weaker and it gets poorer in box 3. The poor correlation in box 3 is not surprising because no creeping fault was introduced in this area in our model. (The creeping segments in our model are the grey thick lines of Figure 6,

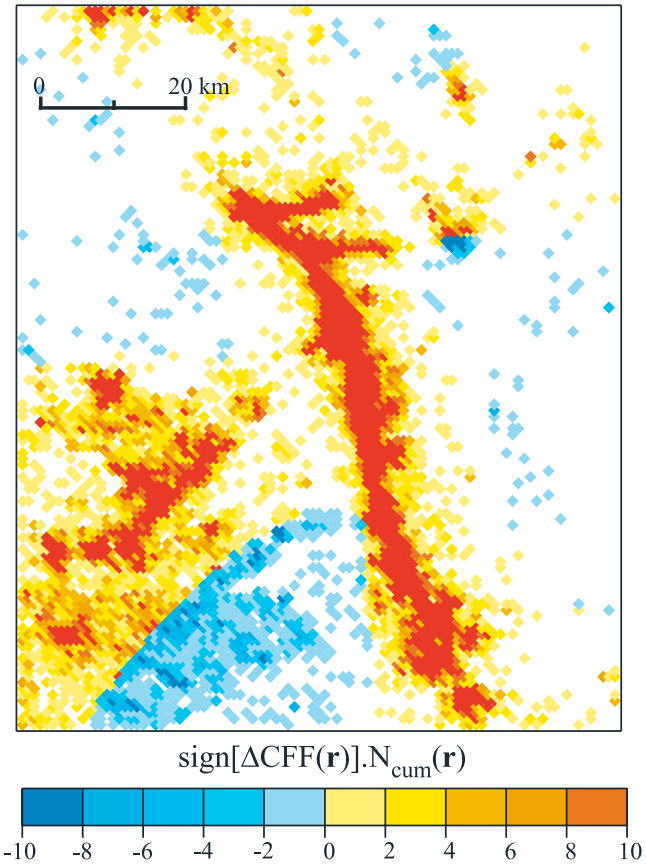

Figure 13. Agreement between the postseismic Coulomb stress change pattern of Figure 10 (center) and the distribution of aftershocks with $M_L > 2$ occurring within 6 years after the main shock. See main text for details.

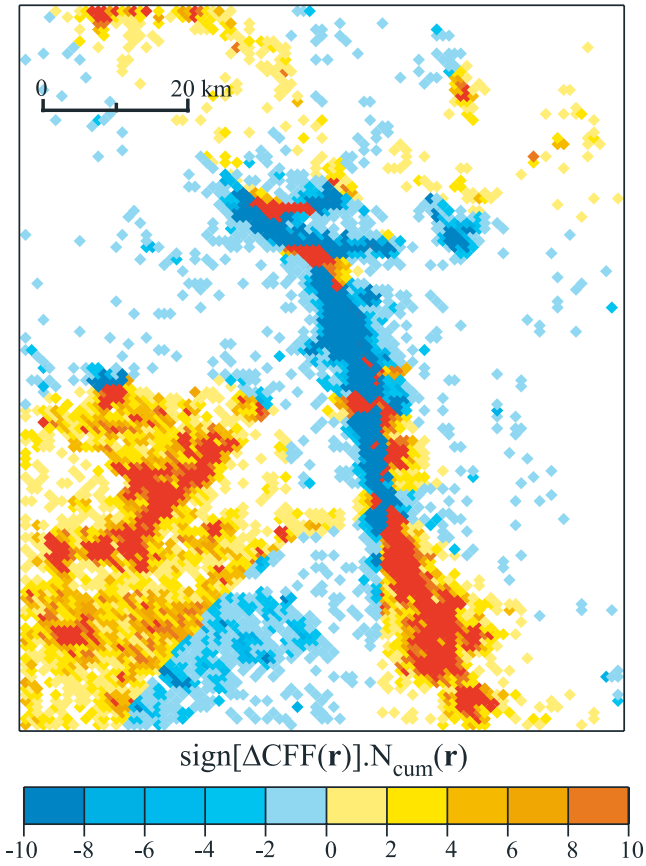

Figure 14. Same as Figure 13 for the coseismic Coulomb stress change pattern of Figure 8.

which are assumed to be restricted to the downdip continuation of the faults that ruptured during the main shocks.) It is possible that some creep also occurred in this area, and introducing a creeping fault there would significantly improve the spatiotemporal correlation between aftershocks and Coulomb stress changes. Unfortunately, there are no good geodetic constraints to assess this possibility.

6. Discussion

6.1. Properties of the BCFZ

[39] In this study, we show that near-field postseismic deformation following the Landers earthquake is well explained by a model in which the coseismic stress changes are relaxed by afterslip in a zone obeying a velocity-strengthening rheology we refer to as the brittle creep fault zone (BCFZ) (see equation (1)). The model depends on an assumed geometry of the BCFZ, and on only four free parameters: (1) The rheological parameter $a\sigma$; (2) the long-term loading velocity V_0; (3) the downdip extent (or width), W_{bcfz}, of the BCFZ; and (4) the effective loading velocity V^- (see section 4.2). We found that it is necessary to distinguish the long-term loading velocity V_0 from the effective (and initial) loading velocity V^-, probably because acceleration of creep might have occurred for reasons other than static stress changes. This creep acceleration may have resulted from viscous relaxation at depth. A factor of 3 acceleration of reloading was proposed by *Pollitz et al.* [2000] based on a viscoelastic model of the postseismic phase of the Landers earthquake. *Perfettini et al.* [2005] found an acceleration of deep viscous flow of about 1.7 for the 2001, M_w8.4 Arequipa earthquake. A factor of 6 increase (as in the best fit model where $V^- = V_0$) is hard to believe, and would be possible only if the viscosity of the ductile part of the fault was very low (10^{18} Pa s) [*Perfettini and Avouac*, 2004b]. This low viscosity is inconsistent with the 10^{19}–10^{20} Pa s range in estimates of the effective dynamic viscosities of the lower crust and upper mantle determined by *Fialko* [2004a]. Consequently, we believe that the "real" model implies an acceleration of both the BCFZ and the ductile faut zone, with the respective contribution of each being difficult to quantify due to the absence of appropriate preseismic geodetic data.

[40] The geometry of the creeping part of the fault zone is not well constrained. The fact that no surface creep was

Table 1. Correlation Between the Coulomb Stress Change Pattern and the Location of Aftershocks

Depth, km	Coseismic	Postseismic
5	58.4%	96.3%
10	60.5%	96.3%
15	41.6%	88.8%

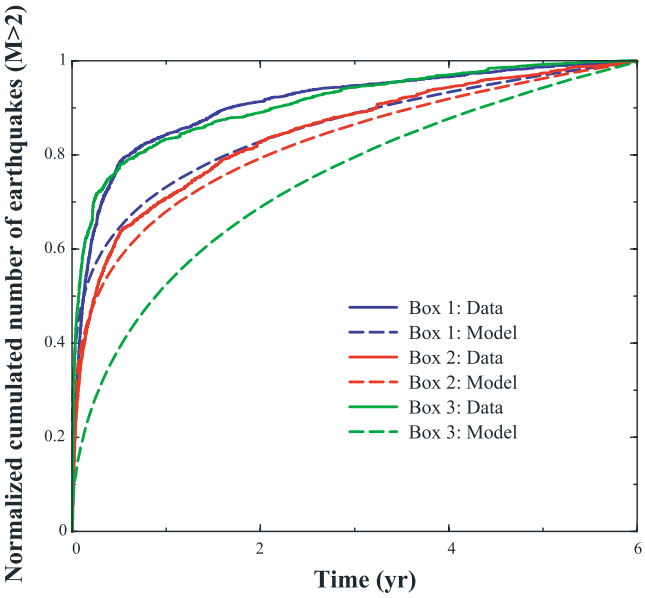

Figure 15. Normalized coulomb stress change computed at the center of the boxes of Figure 11 computed at the bottom of the SFZ together with the normalized cumulative number of aftershocks with $M_W > 2$ in the same boxes. The total number of aftershocks in each box during this 6 year period is 3333 for box 1, 3412 for box 2, and 2219 for box 3.

revealed by field or InSAR investigations, and that a relatively smooth pattern of postseismic velocity revealed by the USGS geodetic array, suggests that afterslip occurred at depth below or comparable to the depth range of coseismic ruptures. In our modeling we have arbitrarily set the upper edge of the BCFZ at 15 km. It may be that afterslip occurred at much shallower depths, with creeping patches interfingered with seismic patches that could have ruptured during the main shock or during the subsequent aftershock sequence. The seismicity lineations observed on the creeping segment of the San Andreas fault show that such interfingering may occur in nature [*Rubin et al.*, 1999].

[41] The frictional parameter is constrained to $d\tau/d\ln V = a\sigma \approx 0.47-0.53$ MPa (equation (1)), at the 67% confidence level. This range is comparable to values estimated from deep afterslip following the Chi-Chi earthquake [*Perfettini and Avouac*, 2004a], the Izmit earthquake [*Hearn et al.*, 2002], and some subduction events [*Perfettini et al.*, 2005; *Hsu et al.*, 2006], which all fall in the range 0.1–1 MPa. The interpretation of $a\sigma$ depends on the rheology considered, namely rate-and-state (RS) or velocity-strengthening (VS) friction, as discussed in Appendix A. If we assume a pure VS friction law, and take into account that afterslip probably occurred at a depth greater than 10 km (where the normal stress must be on the order of 300 MPa or more), we infer $a = a_{VS} \approx 3 \times 10^{-4} - 3 \times 10^{-3}$, where a_{VS} is defined in equation (A4). This value is about one order of magnitude lower than that measured in laboratory experiments (0.005–0.03) [*Blanpied et al.*, 1995; *Chester*, 1995]. One reason for this could be that the effective normal stress within the BCFZ is much lower due to fluid overpressure, as suggested by *Perfettini and Avouac* [2004a] and *Perfettini et al.* [2005]. Another possibility is that the BCFZ is in fact governed by RS rheology, so that $a = a_{RS} - b_{RS}$ (see equation (A3)). Because the top of the BCFZ is a zone that transitions from a rate-strengthening rheology (in the BCFZ) to a rate-weakening one (in the SFZ), we expect $a_{RS} - b_{RS}$ to taper to zero in exactly this part of the BCFZ, so that a could be arbitrarily small in this region (velocity neutral zone). Given that this is where afterslip is maximum due to its proximity to the SFZ, the small value of $a = a_{RS} - b_{RS}$ inferred from our study is consistent with $a_{RS} \rightarrow b_{RS}$ at the top of the BCFZ. We cannot determine which rheology is most appropriate because the predicted postseismic displacement would only differ during an early transient phase of probably quite short duration (on the order of a few days or less, as discussed in Appendix A). Continuous GPS data acquired at high sampling rates (1 Hz) would be necessary to investigate this question.

6.2. Role of Postseismic and Coseismic Stress Transfers in Producing Aftershocks

[42] Our study shows a strong spatial correlation between aftershocks and increased Coulomb stress in the postseismic period, as demonstrated by the observation that aftershocks and postseismic deformation follow about the same temporal evolution (Figure 2). Given that the moment of the aftershocks can only account for a very small fraction of the deformation (the cumulative scalar moment of all the aftershocks of Figure 1 represents only about 3% of the moment needed to explain postseismic deformation), we conclude that reloading by afterslip has governed the spatial distribution and time evolution of aftershocks.

[43] Postseismic relaxation following the Landers earthquake may have particularly contributed to the triggering of the 1999 Hector Mine earthquake. As noticed by *Pollitz and Sacks* [2002], the hypocenter of that event lies in an area where the Coulomb stress did not increase significantly from coseismic deformation induced by the Landers event. Our model predicts that the Coulomb stress increased at the hypocentral location by about 0.04 MPa over the 7 years following the Landers earthquake, and more generally over most of the area that ruptured in 1999. Indeed, we found that the slip distribution of the 1999 Hector Mine earthquake [from *Johnson et al.*, 2002] correlates better with the distribution of postseismic Coulomb stress changes (Figure 16a) than it does with the total (coseismic plus postseismic) Coulomb stress change (Figure 16b). So, we agree with *Pollitz and Sacks* [2002] that postseismic deformation may have contributed to triggering this event, although we ascribe this effect to afterslip rather than to viscoelastic relaxation. In any case, this observation suggests that the appropriate failure criteria for aftershock triggering should depend not only on the static stress but also on the stressing rate, as observed in laboratory experiments of rock failure [*Lockner*, 1998].

[44] This view is quite different from the idea that the temporal evolution of aftershocks is governed by the variation in nucleation times of a fault population governed by rate and state friction in response to coseismic stress changes [*Dieterich*, 1994]. As discussed by *Perfettini and Avouac* [2004a], both models are mathematically identical, although they rely on different physical rationales. In Dieterich's model, the effect of the coseismic stress change is analyzed on a fault population for which the initial velocity

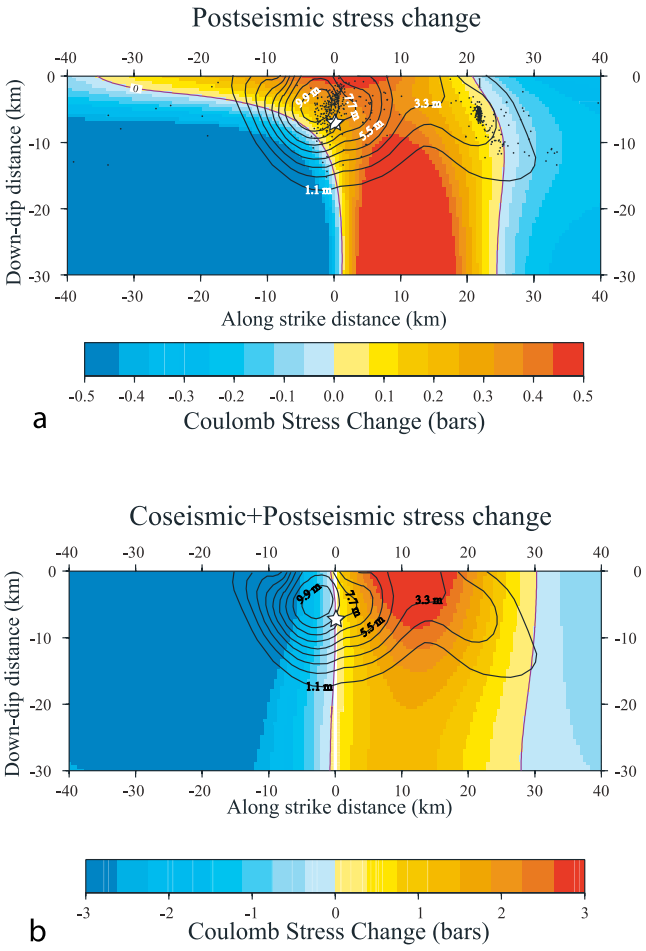

Figure 16. (a) Coulomb stress change induced by 7 years of relaxation after the 1992 Landers earthquake on the fault plane of the 1999 Hector Mine earthquake, whose epicenter is represented by a white star. The coseismic slip distribution is taken from *Johnson et al.* [2002]. (b) Same as Figure 16a for the total (coseismic plus postseismic) Coulomb stress change.

distribution is built to yield a constant seismicity rate in the absence of any stress perturbations. The effect of the main shock is to modify this initial velocity distribution. In this model, the rate of aftershocks depends only on a_{RS} and the duration of an aftershock sequence is given by $t_r^D = a_{RS}\sigma/\dot{\tau}$, $\dot{\tau}$ being the effective stressing rate and $a_{RS}\sigma$ the frictional parameter of equation (A1). Note that in this model, the parameter a_{RS} represents an average value among the faults producing aftershocks. In our model, the parameters involved are all related to the properties of the BCFZ, and the assumption of a constant background seismicity rate is a direct consequence of the return of the BCFZ toward steady state sliding. In Dieterich's model, a coseismic static stress change produces an aftershock sequence of duration t_r^D. The observation that the time evolution of seismicity is in fact consistent with aftershocks being driven by afterslip reloading [*Perfettini and Avouac*, 2004a; *Perfettini et al.*, 2005; *Hsu et al.*, 2006; this study] suggests that our assumption according to which seismicity rate is proportional to postseismic deformation rate is correct. In order to reconcile the two models one has to assume that the faults population responds with insignificant delay to postseismic stress changes so that $t_r \gg t_r^D$.

[45] The near-fault Coulomb stress increase in the postseismic period computed from our afterslip model is in fact significantly smaller (by about a factor of 3) than the coseismic stress reduction computed from the relatively smooth coseismic slip distribution assumed in this study (Figures 8, 9, and 10). This observation implies that the coseismic stress change was much more heterogeneous in the near-fault area, probably due to a rougher slip distribution or a more complex fault geometry than we have assumed, or that aftershocks can occur due to rapid reloading despite a net Coulomb stress decrease.

7. Conclusion

[46] This study shows that the postseismic deformation following the 1992 Landers Earthquake resulted mainly from frictional afterslip (Figures 2, 4, and 6), probably deeper than the seismogenic zone due to the transition with depth from a rate-weakening to a rate-strengthening rheology. The model depends on the geometry of the BCFZ and on free parameters characterizing the friction law; the long-term loading velocity V_0 and the initial postseismic velocity V^-. The parameter V^- appears to be the effective postseismic loading velocity and needs to be much higher than the long-term geological slip rate V_0, possibly because dynamic stresses and deep viscous acceleration may also contribute to acceleration of creep rates along the BCFZ. Reloading of the SFZ by afterslip provides a viable mechanism to explain both the location (Figures 9, 10, and 12) and the time evolution of aftershocks (Figure 15), in particular in the immediate vicinity of the ruptured fault zone where 95% of the aftershocks occurred.

Appendix A: Rate and State Versus Velocity Strengthening

[47] In the rate and state (RS) framework, the frictional stress is given by

$$\tau(t) = \sigma\left[\mu_* + a_{RS}\ln\left(\frac{V(t)}{V_*}\right) + b_{RS}\ln\left(\frac{\theta(t)V_*}{d_c}\right)\right], \qquad \text{(A1)}$$

where a_{RS}, b_{RS}, and μ_* are frictional parameters [*Dieterich*, 1981]. The subscript $(..)_{RS}$ is used to emphasize that those parameters are related to the RS formalism. The state variable θ describes the evolution of the state of the frictional interface. The aging evolution law [*Ruina*, 1983]

$$\frac{d\theta(t)}{dt} = 1 - \frac{V(t)\theta(t)}{d_c}, \qquad \text{(A2)}$$

is often applied where d_c in (A1) and (A2) is the characteristic slip for friction to evolve between two steady states. The frictional stress for sliding at steady state is obtained by imposing $d\theta/dt = 0$ in equation (A1)

$$\tau_{ss}(V) = \sigma\left[\mu_* + (a_{RS} - b_{RS})\ln\left(\frac{V}{V_*}\right)\right]. \qquad \text{(A3)}$$

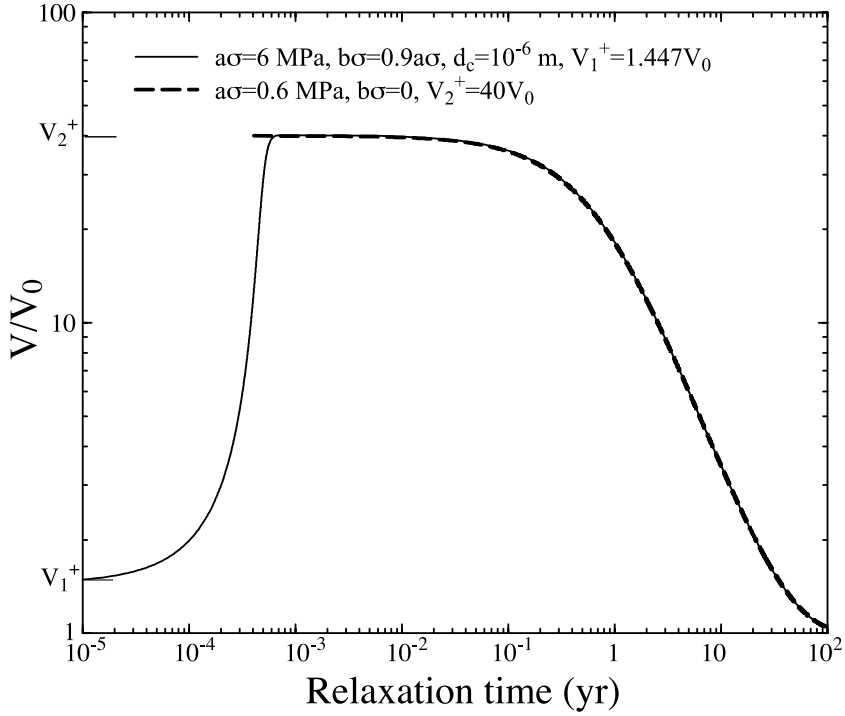

Figure A1. Velocity of a spring slider system in response to an initial step in velocity. Both RS (solid curve) and VS (dashed curve) rheologies are considered. After a transient phase, in the RS case where the velocity increases, both rheologies lead to the same prediction, providing that the parameters of both models are chosen adequately. See main text for discussion.

For postseismic slip it is assumed that $a_{RS} - b_{RS} > 0$, so that the frictional stress increases with velocity and promotes stable sliding.

[48] In steady state, equation (A3) shows that the frictional stress is no longer dependent on the state variable, so that the RS rheology reduces to a pure velocity-strengthening rheology (VS). We then have

$$\tau = \sigma\left[\mu_* + a_{VS}\ln\left(\frac{V}{V_*}\right)\right], a_{VS} > 0, \tag{A4}$$

where $\tau = \tau_{ss}$ and $a_{VS} = a_{RS} - b_{RS}$. The RS and VS formalism will differ only during a transient phase as the fault evolves toward the new steady state (H. Perfettini and J.-P. Ampuero, Dynamics of a velocity strengthening region: Implications for slow earthquakes and postseismic slip, manuscript in preparation, 2006).

[49] When a RS rheology is considered, the rate-strengthening region generates a slip instability in response to a stress perturbation when the characteristic size W_{bcfz} is larger than $L_b = \mu\pi d_c/b_{RS}\sigma$ (H. Perfettini and J.-P. Ampuero, manuscript in preparation, 2006). This instability does not exist for a pure velocity-strengthening region ($b_{RS} = 0$) since, in this case, $L_b \rightarrow \infty$ and the condition $W_{bcfz} > L_b$ is never satisfied. In practice, $W_{bcfz} \gg L_b$ is verified because of the small values of d_c, which is at most a few centimeters [*Marone*, 1998]. This slip instability can be characterized analytically in a 1-D model assuming that the fault is in the self-accelerating phase for which $V\theta/d_c \gg 1$, so that $d\theta/dt \approx -V\theta/d_c$.

[50] Suppose that a static step in shear stress $\Delta\tau$ is applied at time $t = 0$ on a BCFZ sliding at a velocity V^-. The velocity immediately after the stress change at time $t = 0$ is given in the RS framework by

$$V_1 = V^- \exp\left(\frac{\Delta\tau}{a_{RS}\sigma}\right). \tag{A5}$$

When $W_{bcfz} \gg L_b$, the velocity first increases up to the velocity

$$V_2 = V^- \exp\left(\frac{\Delta\tau}{(a_{RS} - b_{RS})\sigma}\right). \tag{A6}$$

This transient phase of increasing slip rate has a duration t^* and ends when the fault first crosses steady state ($d\theta/dt \rightarrow 0$). When $W_{bcfz} \gg L_b$, $t^* \approx (a_{RS}/b_{RS})(d_c/V_1)$, and when $a_{RS} \rightarrow b_{RS}$ b_{RS} like at the top of the BCFZ, $t^* \approx d_c/V_1$ (H. Perfettini and J.-P. Ampuero, manuscript in preparation, 2006).

[51] Figures A1 and A2 show the velocity and displacement, respectively, of a 1-D spring slider system in response to an initial velocity perturbation for RS (continuous curves) and VS (dashed curves) rheologies. For this comparison, we have used model parameters consistent with the modeling, assuming $V^- = V_0 = 7$ mm/yr, a value that may be apt in the case of the fault system that ruptured during the 1992 Landers earthquake. In the VS case, it is assumed that $a_{VS}\sigma = 6$ bar and $V^+_{VS} = 40\ V_0$. For the RS case, it is assumed that $a_{RS} - b_{RS} = a_{VS}$ and $b_{RS} = 0.9\ a_{RS}$, as expected

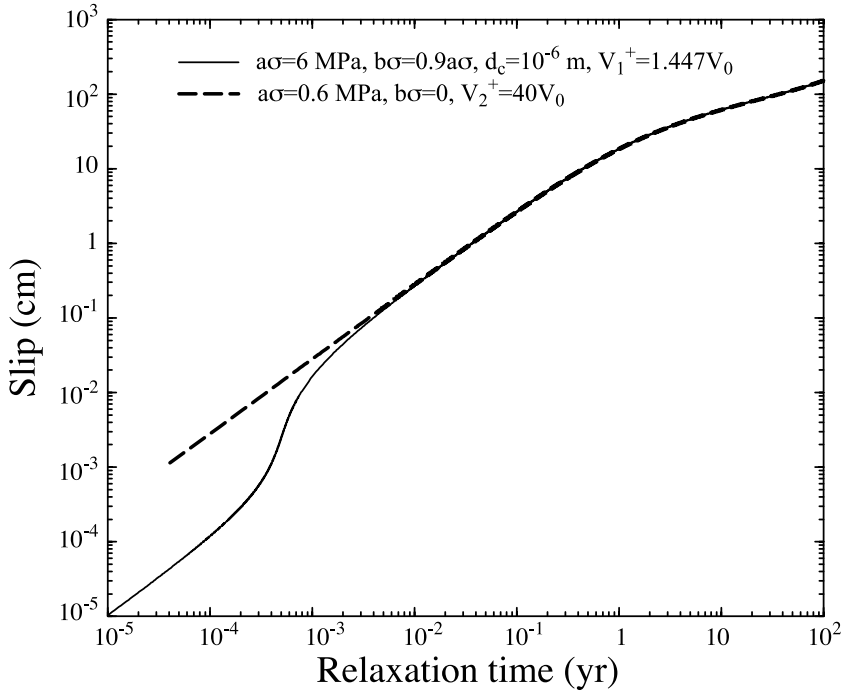

Figure A2. Same as Figure A1 for displacement.

at the top of the BCFZ, and $d_c = 10^{-6}$ m, as suggested by some laboratory measurements [*Marone*, 1998]. It can be verified that in this case $L_b \approx 1.7$ cm $\ll W_{bcfz} = 35$ km, so that the approximation $W_{bcfz} \gg L_b$ is justified. The two formalisms differ up to the time t^*, which is roughly on the order of 10^{-3} years (about 9 hours) with this set of parameters. They become identical at later times, providing that the assumed initial velocity at the onset of postseismic slip in the VS case is equal to the velocity at the end of the transient phase in the RS model. For the example shown here, $V^+_{RS} = V_1 = 1.447\ V_0$ in the RS case and $V^+_{VS} = V_2 = 40\ V_0$ in the VS case. Therefore, for the two models to be equivalent at time $t > t^*$, the initial velocity in the VS case needs to be larger than in the RS case, and the ratio of those two velocities is

$$V_2/V_1 = \exp\left(\frac{\Delta\tau}{(a_{RS} - b_{RS}\sigma)}\right) / \exp\left(\frac{\Delta\tau}{a_{RS}\sigma}\right).$$

When $b_{RS} \rightarrow a_{RS}$, this ratio could be arbitrarily large. Therefore, except during the transient phase of duration t^*, VS and RS are equivalent.

[52] Since $t^* \approx d_c/V_1$ when $b_{RS} \rightarrow a_{RS}$, we find using $d_c = 10^{-2}$–10^{-6} m [*Marone*, 1998] and the lower bound $V_1 = V_0 = 7$ mm/yr, that $t^* = 10^{-4} - 1$ years. Consequently, it is only in the case of a large value of d_c (millimetric or more) that such a transition phase may be detected by GPS measurements. Since the first GPS campaign data were collected 12 days after the event, it is not surprising that this transient phase (assuming that RS rheology applies in the case of Landers) is not observed in the data. Consequently, we will consider in this study a VS rheology as expressed in equation (1), keeping in mind that the real rheology might in fact involve a state variable that implies a transient phase not correctly modeled by VS rheology.

Appendix B: Link Between Our Model and Viscoelastic Models

[53] Viscoelastic models are often proposed to explain postseismic slip (see, for example, *Deng et al.* [1998], *Pollitz et al.* [2000], and *Fialko* [2004a] for the case of the Landers earthquake). They usually describe well the long-term postseismic slip, but fail to describe the short-term response [*Deng et al.*, 1998]. It could be that the viscoelastic models only apply at great depths (say for temperatures higher than 600°C), and that it takes a significant time for postseismic slip to reach those depths.

[54] The viscous stress rate $d\tau_\eta/dt$ for a Newtonian fluid is given by

$$\frac{d\tau_\eta}{dt} = \frac{\eta}{\Delta h}\frac{dV}{dt}, \tag{B1}$$

where η is the effective viscosity, dV/dt the sliding acceleration, and Δh the characteristic thickness of the viscous shear zone. According to equation (3), the frictional stress rate considering a velocity-strengthening rheology is given by $d\tau_f/dt = (a\sigma/V)\ (dV/dt)$. For an infinitesimal stress perturbation, $V \approx V_0$, and

$$\frac{d\tau_f}{dt} \approx \frac{a\sigma}{V_0}\frac{dV}{dt}. \tag{B2}$$

So at great depths, where the coseismic stress changes (and hence the velocity changes) are small, VS rheology reduces

to a linear viscous rheology (LV). This may explain the success of the model in accounting for deep postseismic slip, or, equivalently, the long-term evolution of postseismic slip.

[55] Identifying (B1) and (B2) leads to the following correspondence between VS and LV rheologies

$$\frac{a\sigma}{V_0} \approx \frac{\eta}{\Delta h}. \tag{B3}$$

In particular, the relaxation time predicted by a 1-D model of a relaxing BCFZ is $t_r = a\sigma/KV_0$, where K is the stiffness of the fault [*Perfettini and Avouac*, 2004a]. Using (B3), this relaxation time transforms into $t_\eta = \eta/K\Delta h$, which is the well-known Maxwell time of LV rheology.

[56] Taking $\eta = 10^{19}$ Pa s as in the viscoelastic model of *Fialko* [2004a], we found that for our best fit model ($a\sigma \approx$ 5 bars and $V_0 = 2$ mm/yr), $\Delta h = \eta V_0/a\sigma \approx 1.3$ km. This value should be considered as relevant only in the approximation of infinitesimal perturbations for which $V \approx V_0$. Consequently, it should only apply to the bottom of the BCFZ, where the coseismic stress changes are small compared to $a\sigma$. The results suggest that at great depths (say 60 km in the case of the Landers earthquake), deformation could be distributed over kilometer-scale widths.

[57] **Acknowledgments.** We are very grateful to J. C. Savage and Y. Fialko for providing us with some of the materials used in this study. We thank Y. Fialko and A. Rubin for their constructive reviews which have really helped us to clarify some key assumptions of the model. We have also benefited from discussions with J.-P. Ampuero and S. Mazzotti. We thank H. G. Steele and E. Nadin for language corrections. Some of the figures in this paper were made using Generic Mapping Tools (GMT) [*Wessel and Smith*, 1998]. This work has been partially funded by IRD. This is Caltech Tectonics Observatory contribution 69.

References

Amelung, F., and J. W. Bell (2003), Interferometric synthetic aperture radar observations of the 1994 Double Spring Flat, Nevada, earthquake (M5.9): Main shock accompanied by triggered slip on a conjugate fault, *J. Geophys. Res.*, *108*(B9), 2433, doi:10.1029/2002JB001953.

Amitrano, D., and A. Helmstetter (2006), Brittle creep, damage, and time to failure in rocks, *J. Geophys. Res.*, *111*, B11201, doi:10.1029/2005JB004252.

Blanpied, M. L., D. A. Lockner, and J. D. Byerlee (1995), Frictional slip of granite at hydrothermal conditions, *J. Geophys. Res.*, *100*, 13,045–13,064.

Bock, Y., et al. (1997), Southern California permanent GPS geodetic array: Continuous measurements of regional crustal deformation between the 1992 landers and 1994 Northridge earthquakes, *J. Geophys. Res.*, *102*, 18,013–18,033.

Bodin, P., R. Bilham, J. Behr, J. Gomberg, and K. Hudnut (1994), Slip triggered on southern California faults by the 1992 Joshua Tree, Landers, and Big Bear earthquakes, *Bull. Seismol. Soc. Am.*, *84*, 806–816.

Bosl, W. J., and A. Nur (2002), Aftershocks and pore fluid diffusion following the 1992 Landers earthquake, *J. Geophys. Res.*, *107*(B12), 2366, doi:10.1029/2001JB000155.

Bouchez, J., C. Mariotti, M. Flouzat, C. Antoine, D. Buigues, and P. Denier (1996), Structural integrity and stability of the atolls: Data and modeling, in *Geomechanical and Radiological Impact of Nuclear Tests at Mururoa and Fangataufa (French Polynesia)*, vol. 2, pp. 512–594, Doc. Fr., Paris.

Chester, F. (1995), A rheologic model for wet crust applied to strike-slip faults, *J. Geophys. Res.*, *100*, 13,033–13,044.

Cocks, A. C. F., and A. R. S. Ponter (Eds.) (1989), *Mechanics of Creep Brittle Materials*, Springer, New York.

Cruden, D. M. (1970), A theory of brittle creep in rock under uniaxial compression, *J. Geophys. Res.*, *75*, 3431–3441.

Deng, J., M. Gurnis, M. Kanamori, and E. Hauksson (1998), Viscoelastic flow in the lower crust after the 1992 Landers, California earthquake, *Science*, *282*, 1689–1692.

Dieterich, J. H. (1981), Constitutive properties of faults with simulated gouge, in *Mechanical Behavior of Crustal Rocks*, *Geophys. Monogr. Ser.*, vol. 24, edited by N. L. Carter et al., pp. 103–120, AGU, Washington, D. C.

Dieterich, J. H. (1994), A constitutive law for rate of earthquake production and its application to earthquake clustering, *J. Geophys. Res.*, *99*, 2601–2618.

Dragert, H., K. Wang, and T. James (2001), A silent slip event on the deeper Cascadia subduction interface, *Science*, *292*, 1525–1528.

Fialko, Y. (2004a), Evidence of fluid-filled upper crust from observations of postseismic deformation due to the 1992 M_w7.3 Landers earthquake, *J. Geophys. Res.*, *109*, B08401, doi:10.1029/2004JB002985.

Fialko, Y. (2004b), Probing the mechanical properties of seismically active crust with space geodesy: Study of the coseismic deformation due to the 1992 M_w 7.3 Landers (southern California) earthquake, *J. Geophys. Res.*, *109*, B03307, doi:10.1029/2003JB002756.

Goldberg, D. (1989), *Genetic Algorithms in Search, Optimization, and Machine Learning*, Addison-Wesley, Boston, Mass.

Gordon, D., C. Ma, and J. Ryan (1993), Results from the CDP Mobile VLBI Program in the western United states, in *Contribution of Space Geodesy to Geodynamics: Crustal Dynamics*, *Geodyn. Ser.*, vol. 23, edited by D. Smith and D. Turcotte, pp. 131–138. AGU, Washington, D. C.

Gross, S., and C. Kisslinger (1997), Estimating tectonic stress rate and state with Landers aftershocks, *J. Geophys. Res.*, *102*, 7603–7612.

Hardebeck, J., and E. Hauksson (2001), Crustal stress field in southern California and its implications for fault mechanics, *J. Geophys. Res.*, *106*, 21,859–21,882.

Hardebeck, J., J. Nazareth, and E. Hauksson (1998), The static stress change triggering model: Constraints from the southern California aftershock sequences, *J. Geophys. Res.*, *103*, 24,427–24,437.

Hauksson, E., W.-C. Chi, P. Shearer, and A. Michael (2003), Comprehensive waveform cross-correlation of southern California seismograms: part 1. Refined hypocenters obtained using the double-difference method and tectonic implications, *Eos Trans. AGU*, *84*(46), Fall Meet. Suppl., Abstract S21D-0325.

Hearn, E., R. Burgmann, and R. Reilinger (2002), Dynamics of Izmit earthquake postseismic deformation and loading of the Duzce earthquake hypocenter, *Bull. Seismol. Soc. Am.*, *92*, 172–193.

Hsu, Y., N. Bechor, P. Segall, S. Yu, L. Kuo, and K. Ma (2002), Rapid afterslip following the 1999 Chi-Chi, Taiwan earthquake, *Geophys. Res. Lett.*, *29*(16), 1754, doi:10.1029/2002GL014967.

Hsu, Y.-J., M. Simons, J.-P. Avouac, J. Galetzka, K. Sieh, M. Chlieh, D. Natawidjaja, L. Prawirodirdjo, and Y. Bock (2006), Frictional afterslip following the 2005 Nias-Simeulue earthquake, Sumatra, *Science*, *312*, 1921–1926.

Hudnut, K., and M. Clark (1989), New slip along parts of the 1968 Coyote Creek fault rupture, California, *Bull. Seismol. Soc. Am.*, *79*, 451–465.

Johnson, S., H. Zebker, P. Segall, and F. Amelung (2002), Fault slip distribution of the 1999 M_w7.1 Hector Mine, California, earthquake estimated from satellite radar and GPS measurements, *Bull. Seismol. Soc. Am.*, *92*, 1377–1389.

King, G. C. P., R. S. Stein, and J. Lin (1994), Static stress changes and the triggering of earthquakes, *Bull. Seismol. Soc. Am.*, *84*, 935–953.

Lachenbruch, A. H., and J. H. Sass (1973), Thermo-mechanical aspects of the San Andreas, in *Proceedings, Conference on the tectonic problems of the San Andreas fault system*, edited by R. L. Kovach and A. Nur, *Stanford Univ. Publ. Sci.*, *13*, 192–205.

Langbein, J., J. Murray, and H. Snyder (2006), Coseismic and initial postseismic deformation from the 2004 Parkfield, California earthquake, observed by GPS, EDM, creepmeters, and borehole strainmeters, *Bull. Seismol. Soc. Am.*, *96*, S304–S320, doi:10.1785/0120050823.

Lapusta, N., and J. R. Rice (2003), Nucleation and early seismic propagation of small and large events in a crustal earthquake model, *J. Geophys. Res.*, *108*(B4), 2205, doi:10.1029/2001JB000793.

Liu, J., K. Sieh, and E. Hauksson (2003), A structural interpretation of the aftershock "cloud" of the 1992 M_w7.3 Landers earthquake, *Bull. Seismol. Soc. Am.*, *93*, 1333–1344.

Lockner, D. A. (1998), A generalized law for brittle deformation of Westerly granite, *J. Geophys. Res.*, *103*, 5107–5123.

Marone, C. (1998), Laboratory-derived friction laws and their application to seismic faulting, *Annu. Rev. Eath Planet. Sci.*, *26*, 643–696.

Marone, C. J., C. H. Scholz, and R. Bilham (1991), On the mechanics of earthquake afterslip, *J. Geophys. Res.*, *96*, 8441–8452.

Massonnet, D., W. Thatcher, and H. Vadon (1996), Detection of postseismic fault-zone collapse following the Landers earthquake, *Nature*, *382*, 612–616.

Miyazaki, S., P. Segall, J. Fukuda, and T. Kato (2004), Space time distribution of afterslip following the 2003 Tokachi-oki earthquake: Implications for variations in fault zone frictional properties, *Geophys. Res. Lett.*, *31*, L06623, doi:10.1029/2003GL019410.

Montési, L. G. J. (2004), Controls of shear zone rheology and tectonic loading on postseismic creep, *J. Geophys. Res.*, *109*, B10404, doi:10.1029/2003JB002925.

Nelder, J. A., and R. Mead (1965), A simplex method for function minimization, *Comput. J.*, *7*, 308–313.
Okada, Y. (1992), Internal deformation due to shear and tensile faults in a half-space, *Bull. Seismol. Soc. Am.*, *82*, 1018–1040.
Peltzer, G., P. Rozen, F. Rogez, and K. Hudnut (1996), Postseismic rebound in fault step-overs caused by pore fluid flow, *Science*, *272*, 1202–1204.
Peltzer, G., P. Rozen, F. Rogez, and K. Hudnut (1998), Poroelastic rebound along the Landers 1992 earthquake surface rupture, *J. Geophys. Res.*, *103*, 30,131–30,145.
Perfettini, H., and J.-P. Avouac (2004a), Postseismic relaxation driven by brittle creep: A possible mechanism to reconcile geodetic measurements and the decay rate of aftershocks, application to the Chi-Chi earthquake, Taiwan, *J. Geophys. Res.*, *109*, B02304, doi:10.1029/2003JB002488.
Perfettini, H., and J.-P. Avouac (2004b), Stress transfer and strain rate variations during the seismic cycle, *J. Geophys. Res.*, *109*, B06402, doi:10.1029/2003JB002917.
Perfettini, H., J. Schmittbuhl, and A. Cochard (2003a), Shear and normal load perturbations on a two-dimensional continuous fault: 1. Static triggering, *J. Geophys. Res.*, *108*(B9), 2408, doi:10.1029/2002JB001804.
Perfettini, H., J. Schmittbuhl, and A. Cochard (2003b), Shear and normal load perturbations on a two-dimensional continuous fault: 2. Dynamic triggering, *J. Geophys. Res.*, *108*(B9), 2409, doi:10.1029/2002JB001805.
Perfettini, H., J.-P. Avouac, and J.-C. Ruegg (2005), Geodetic displacements and aftershocks following the 2001 M_w = 8.4 Peru earthquake: Implications for the mechanics of the earthquake cycle along subduction zones, *J. Geophys. Res.*, *110*, B09404, doi:10.1029/2004JB003522.
Pollitz, F., and I. Sacks (2002), Stress triggering of the 1999 Hector Mine earthquake by transient deformation following the 1992 Landers earthquake, *Bull. Seismol. Soc. Am.*, *92*, 1487–1496.
Pollitz, F., R. Burgmann, and P. Segall (1998), Joint estimation of afterslip rate and postseismic relaxation following the 1989 Loma Prieta earthquake, *J. Geophys. Res.*, *103*, 26,975–26,992.
Pollitz, F., G. Peltzer, and R. Burgmann (2000), Mobility of continental mantle: Evidence from postseismic geodetic observations following the 1992 Landers earthquake, *J. Geophys. Res.*, *105*, 8035–8054.
Press, W. H., B. P. Flannery, S. A. Teukolsky, and W. T. Vetterling (1992), Simulated annealing methods, in *Numerical Recipes in C, The Art of Scientific Computing*, 2nd ed., pp. 451–455, Cambridge Univ. Press, Cambridge, U. K.
Rice, J. R. (1993), Spatio-temporal complexity of slip on a fault, *J. Geophys. Res.*, *98*, 9885–9907.
Rice, J. R., and J. Gu (1983), Earthquake aftereffects and triggered seismic phenomena, *Pure Appl. Geophys.*, *121*, 187–219.
Rubin, A. M., D. Gillard, and J.-L. Got (1999), Microseismic lineations along creeping faults, *Nature*, *400*, 635–641.
Rubin, C., and K. Sieh (1997), Long dormancy, low slip rate and similar slip-per-event for the Emerson Fault, eastern California shear zone, *J. Geophys. Res.*, *102*, 15,319–15,335.
Ruina, A. L. (1983), Slip instability and state variable fricton laws, *J. Geophys. Res.*, *88*, 10,359–10,370.
Sauber, J., W. Tatcher, and S. Solomon (1986), Geodetic measurement of deformation in central Mojave desert, California, *J. Geophys. Res.*, *91*, 12,683–12,693.
Sauber, J., W. Tatcher, S. Solomon, and M. Lisowski (1994), Geodetic slip rate for the eastern California shear zone and the recurrence time of Mojave desert earthquakes, *Nature*, *367*, 264–266.
Savage, J., and J. Svarc (1997), Postseismic deformation associated with the 1992 M_w = 7.3 Landers earthquake, southern California, *J. Geophys. Res.*, *102*, 7565–7577.
Savage, J., M. Lisowski, and W. Prescott (1990), An apparent shear zone trending north-northwest across the Mojave Desert into Owens Valley, eastern California, *Geophys. Res. Lett.*, *17*, 2113–2116.
Savage, J. C., J. L. Svarc, and W. H. Prescott (2003), Near-field postseismic deformation associated with the 1992 Landers and 1999 Hector Mine, California, earthquakes, *J. Geophys. Res.*, *108*(B9), 2432, doi:10.1029/2002JB002330.
Savage, J. C., J. L. Svarc, and S.-B. Yu (2005), Postseismic relaxation and transient creep, *J. Geophys. Res.*, *110*, B11402, doi:10.1029/2005JB003687.
Scholz, C. (1968), Mechanism of creep in brittle rock, *J. Geophys. Res.*, *73*, 3295–3302.
Scholz, C. H. (2002), *The Mechanics of Earthquakes and Faulting*, Cambridge Univ. Press, New York.
Shen, Z.-K., D. Jackson, Y. Feng, M. Cline, M. Kim, P. Fang, and Y. Bock (1994), Postseismic deformation following the Landers earthquake, California, 28 June 1992, *J. Geophys. Res.*, *84*, 780–791.
Smith, S., and M. Wyss (1968), Displacement on the San Andreas fault subsequent to the 1966 parkfield earthquake, *Bull. Seismol. Soc. Am.*, *58*, 1955–1973.
Stein, R. (1999), The role of stress transfer in earthquake occurrence, *Nature*, *402*, 605–609.
Wessel, P., and W. H. F. Smith (1998), New, improved version of the Generic Mapping Tools released, *Eos Trans. AGU*, *79*, 579.
Zweck, C., J. T. Freymueller, and S. C. Cohen (2002), Three-dimensional elastic dislocation modeling of the postseismic response to the 1964 Alaska earthquake, *J. Geophys. Res.*, *107*(B4), 2064, doi:10.1029/2001JB000409.

J.-P. Avouac, Tectonics Observatory, California Institute of Technology, Mail code 100-23, Pasadena, CA 91125, USA. (avouac@gps.caltech.edu)
H. Perfettini, Institut de Recherche pour le Développement/Observatoire Midi-Pyrénées, 14 avenue Edouard Belin, F-31400 Toulouse, France. (hugo.perfettini@ird.fr)